

**Department of Physics and Astronomy  
University of Heidelberg**

Master Thesis in Physics  
submitted by

**Jan Dreher**

born in Ravensburg (Germany)

**2022**



# **A Microwave Power Stabilization Setup for Controlling Spin Dynamics in a Bose-Einstein Condensate**

This Master Thesis has been carried out by Jan Dreher at the  
Kirchhoff-Institute for Physics in Heidelberg  
under the supervision of  
Prof. Dr. Markus K. Oberthaler

## Abstract

### **A Microwave Power Stabilization Setup for Controlling Spin Dynamics in a Bose-Einstein Condensate**

This thesis presents the setup and testing of a microwave power stabilization utilized for an increased level of control over the spin dynamics in a  $^{87}\text{Rb}$  Bose-Einstein condensate in the  $F = 1$  hyperfine manifold where the magnetic sublevels constitute a spin-1 system with ferromagnetic interactions. By applying off-resonant microwave dressing, we are able to tune the effective quadratic Zeeman shift and obtain an experimental control parameter for the spin dynamics. To achieve a long-term stable operation of the control parameter, we construct a power stabilization for the microwave signal, aiming to reduce fluctuations in the short-term up to  $\sim 10$  kHz and slow drifts in the long-term. Here, we report on the setup of this stabilization and benchmark its performance in a test setup as well as with the stability of Rabi oscillations in the Bose-Einstein condensate. The setup accomplishes a power stability of  $10^{-4}$  over short time scales ( $< 1$  h) and reaches a stability of  $\sim 4 \cdot 10^{-4}$  over longer time frames ( $\sim 1$  day).

## Zusammenfassung

### **Ein Aufbau zur Stabilisierung der Mikrowellenleistung für die Kontrolle über die Spin-Dynamik in einem Bose-Einstein Kondensat**

Diese Arbeit präsentiert den Aufbau und Tests einer Stabilisierung der Mikrowellenleistung. Diese wird verwendet für eine bessere Kontrolle über die Spin-Dynamik in einem  $^{87}\text{Rb}$  Bose-Einstein Kondensat im  $F = 1$  Hyperfeinstruktur-Niveau, wo die magnetischen Sub-Level ein Spin-1 System mit ferromagnetischen Wechselwirkungen bilden. Durch nicht-resonantes Mikrowellen dressing können wir den effektiven quadratischen Zeeman-Effekt beeinflussen und erhalten somit einen experimentellen Kontrollparameter für die Spin-Dynamik. Um eine langfristig stabile Operation des Kontrollparameters zu erreichen, haben wir eine Stabilisierung für die Leistung des Mikrowellensignals konstruiert, welche schnelle Fluktuationen bis zu  $\sim 10$  kHz und langsame Drifts reduzieren soll. Hier erläutern wir den Aufbau dieser Stabilisierung und überprüfen dessen Funktionsweise in einem Testaufbau sowie durch die Stabilität von Rabi Oszillationen in dem Bose-Einstein Kondensat. Der Aufbau erreicht eine Stabilität von  $10^{-4}$  über kurze Zeitskalen ( $< 1$  h) und  $\sim 4 \cdot 10^{-4}$  für längere Zeitskalen ( $\sim 1$  Tag).

# Contents

<b>1</b>	<b>Introduction</b>	<b>7</b>
<b>2</b>	<b>Theoretical background</b>	<b>8</b>
2.1	Two-level system in the dressed atom picture . . . . .	8
2.2	Spin-1 system . . . . .	10
2.2.1	Single particle description . . . . .	10
2.2.2	Many-body limit . . . . .	12
<b>3</b>	<b>Experimental system</b>	<b>13</b>
3.1	BEC generation and trapping potential . . . . .	13
3.2	Level structure . . . . .	14
3.3	Interactions in a spin-1 system . . . . .	16
3.4	Internal control . . . . .	18
3.5	Mean-field phase diagram . . . . .	20
3.6	Typical experimental run . . . . .	21
3.7	Readout . . . . .	22
<b>4</b>	<b>Microwave stabilization</b>	<b>24</b>
4.1	Motivation . . . . .	24
4.2	Microwave system . . . . .	24
4.2.1	Power stabilization . . . . .	25
4.2.2	Temperature stabilization . . . . .	29
4.3	Noise analysis in a test setup . . . . .	31
4.4	Stability measurement with Rabi oscillations . . . . .	36
4.4.1	Long-term drifts . . . . .	39
4.4.2	Microwave gradient . . . . .	41
<b>5</b>	<b>Impact of <math>q</math> on the spin dynamics</b>	<b>43</b>
5.1	Spectroscopy . . . . .	43
5.2	Gap measurement . . . . .	45
<b>6</b>	<b>Outlook</b>	<b>49</b>
<b>A</b>	<b>Additional figures</b>	<b>51</b>
	<b>Bibliography</b>	<b>55</b>



# 1 Introduction

Initiated by the first realization of a Bose-Einstein condensate (BEC) in a dilute ultra-cold gas [1] [2], the experimental study of quantum many-body behavior has seen tremendous progress. In these systems, many interesting phenomena can be investigated which are, among others, superfluidity, quantum vortices, entanglement and the development of quantum technologies. Particularly desirable is a system in which every parameter occurring in the Hamiltonian can be modified, much like in the concept of a quantum simulator, hence allowing to study synthetic quantum systems.

Our experimental system is a spinor BEC of  $^{87}\text{Rb}$  occupying the  $F = 1$  hyperfine manifold where the magnetic sublevels constitute a spin-1 system featuring ferromagnetic interactions. Interatomic spin-changing collisions can redistribute pairs of particles between the magnetic substates and induce quantum correlations in the system. The occurrence of these spin-spin interactions depends on the energy shift of the internal levels. We employ off-resonant microwave dressing to tune this energy shift and therefore obtain an experimental control parameter for the spin dynamics in our system. Given this experimental platform, a variety of quantum many-body phenomena can be explored. For instance, quenching the system over a quantum phase transition thereby driving it far from equilibrium leads to the emergence of self-similar behavior [3]. Furthermore, the spin-changing collisions can be used to generate multipartite entanglement [4]. Independently of the phenomenon that is investigated, a robust operation of the entire experimental apparatus has to be ensured. A stable microwave dressing is of particular importance.

In this thesis we present the setup and characterization for an power stabilization of a microwave signal which aims for long-term stability. The setup is independent of the microwave source. We start by introducing some important theoretical concepts in chapter 2, before an overview of the experimental system is given in chapter 3, where we also discuss the properties of the many-body spin-1 system in more detail and show the typical experimental procedure. In chapter 4, the microwave system is described and the stabilization setup of the microwave signal is discussed in detail and its performance is analyzed by directly measuring the microwave power and by observing fluctuations of the Rabi coupling in the condensate. In chapter 5 we demonstrate how the microwave dressing affects the internal state of the many-body system by examining the spin dynamics in dependence of this control parameter. Finally, we conclude with a brief outlook in chapter 6.

## 2 Theoretical background

In this chapter we want to discuss some basic theoretical concepts which will be useful throughout this thesis. We start by reviewing the interaction of a two-level atom with an electromagnetic field, before we take a look at the description of spin-1 particles.

### 2.1 Two-level system in the dressed atom picture

The interaction of a two-level atom with a radiation field is frequently discussed in the literature with various approaches. Here, we want to use the dressed atom picture as given in [5] where the Hamiltonian of the system is

$$\hat{\mathcal{H}} = \hat{\mathcal{H}}_a + \hat{\mathcal{H}}_f + \hat{\mathcal{H}}_{af} \quad (2.1)$$

where  $\hat{\mathcal{H}}_a$  and  $\hat{\mathcal{H}}_f$  are the energies of the atom and the field respectively, while  $\hat{\mathcal{H}}_{af}$  describes the atom-field interaction. We consider a simple two-level atom consisting of a ground state  $|g\rangle$  and an excited state  $|e\rangle$  which are split by the energy difference  $\Delta E = \hbar\omega$ . When we define the energy of the ground state to be zero,  $\hat{\mathcal{H}}_a$  is given by

$$\hat{\mathcal{H}}_a = \hbar\omega |e\rangle \langle e| \quad (2.2)$$

Further, the field is introduced in a fully quantized version where only a single mode of the electromagnetic field with frequency  $\omega_l$  is considered such that the field Hamiltonian is

$$\hat{\mathcal{H}}_f = \hbar\omega_l \left( \hat{a}^\dagger \hat{a} + \frac{1}{2} \right) \quad (2.3)$$

with  $\hat{a}^\dagger$  being the creation and  $\hat{a}$  the annihilation operators. The field is then conveniently expressed in terms of the Fock state  $|N\rangle$ , where  $N$  is the number of photons in the mode  $\omega_l$ .

#### Bare States

For the beginning, we neglect the interaction term ( $\hat{\mathcal{H}}_{af} = 0$ ). The Hilbert space then simply contains the atomic as well as the electromagnetic field states, which makes it convenient to express them in a combined product state of the form  $|e/g, N\rangle$ . The energy scheme of the product states is shown in Fig. 2.1 a). In the case of small detuning  $|\delta| = |\omega - \omega_l| \ll \omega$  the ground state with  $N + 1$  photons  $|g, N + 1\rangle$  is almost degenerate with the excited state with  $N$  photons  $|e, N\rangle$ . We group those two states together in the manifold  $\Sigma(N)$ .

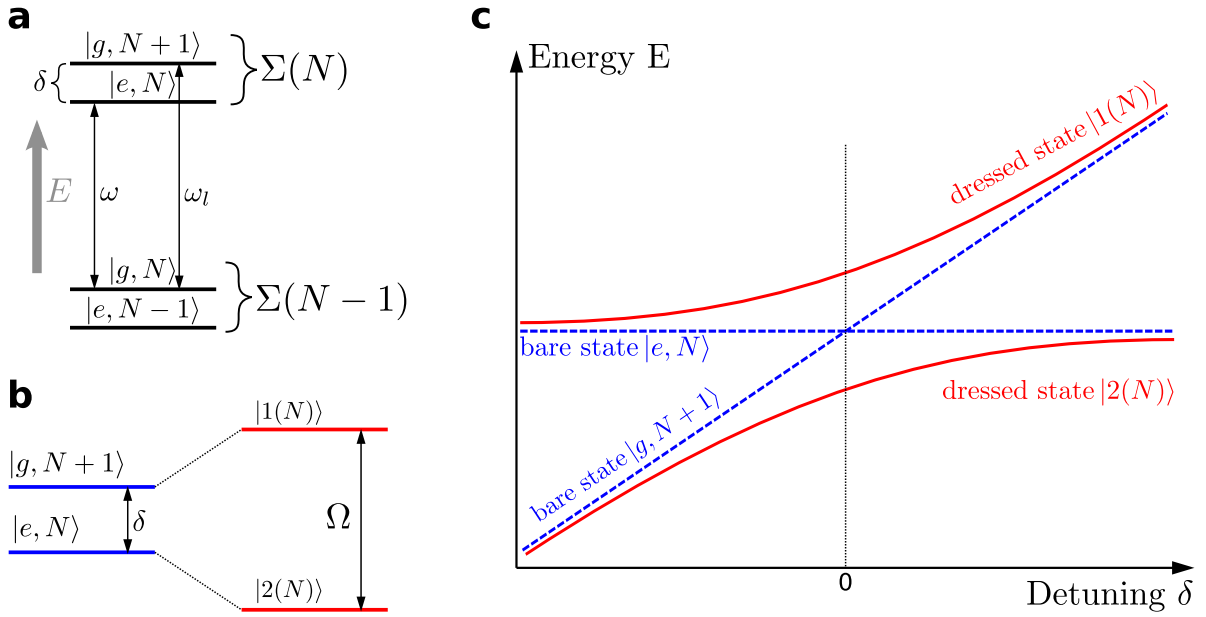


**Figure 2.1 Dressed-atom level structure.** **a)** Neglecting the atom-field interaction yields the bare states. These represent a product states of the atomic and the field state and can be grouped into manifolds  $\Sigma(N)$ . **b)** When we take the interaction into account, the energy splitting of the two states within a manifold is increased. We find the new eigenstates  $|1(N)\rangle$  and  $|2(N)\rangle$  which are called dressed states. **c)** The energy of the bare and the dressed states are shown in dependence of the detuning. Through the interaction, the level-crossing of the bare states at  $\delta = 0$  turns into an avoided crossing for the dressed states.

## Dressed States

Now, we introduce the atom-field interaction in the electric dipole approximation where we assume that the field is uniform over the entire atom. The interaction Hamiltonian is then

$$\hat{\mathcal{H}}_{af} = -\hat{\mathbf{D}} \cdot \hat{\mathbf{E}} \quad (2.4)$$

with the electric dipole operator

$$\hat{\mathbf{D}} = \mathbf{d} (|g\rangle \langle e| + |e\rangle \langle g|) \quad (2.5)$$

where  $\mathbf{d} = e\mathbf{r}$  is the atomic dipole moment and  $\mathbf{r}$  is the position vector of the electron. The electric field at the position of the atom is

$$\hat{\mathbf{E}} = \sqrt{\frac{\hbar\omega_l}{2\epsilon_0 V}} \hat{\epsilon}_l (\hat{a} + \hat{a}^\dagger) \quad (2.6)$$

Substituting eq. (2.5) and (2.6) into the interaction Hamiltonian yields

$$\hat{\mathcal{H}}_{af} = g (|e\rangle \langle g| \hat{a} + \hat{a}^\dagger |g\rangle \langle e|) \quad (2.7)$$

where we defined the coupling constant  $g = -\hat{\epsilon}_l \mathbf{d} \sqrt{\frac{\hbar\omega_l}{2\epsilon_0 V}}$ . The first term describes the excitation of the atom from the ground to the excited state combined with an annihilation of one photon,

while the second term describes the opposite process. In eq. (2.7) we have neglected the terms  $|e\rangle\langle g|\hat{a}^\dagger$  and  $|g\rangle\langle e|\hat{a}$  which describe the process in which the atom is excited and a photon is created and the opposite. Both terms do not conserve energy and neglecting them corresponds to making the rotating-wave approximation.

We find that the atom-field interaction term leads to a coupling of the two states within each manifold  $\Sigma(N)$

$$\langle e, N | \hat{\mathcal{H}}_{af} | g, N + 1 \rangle = g\sqrt{N + 1} \quad (2.8)$$

Now, we further assume that the photon number  $N$  is very large and fluctuations of it can be neglected. This effectively introduces a classical field  $\mathcal{E}$  which allows us to express the coupling in eq. (2.8) independent from  $N$  [6]. The two-level system given in each manifold  $\Sigma(N)$  can then be described by the following Hamiltonian

$$\hat{\mathcal{H}} = \frac{\hbar}{2} \begin{pmatrix} -\delta & \Omega_0 \\ \Omega_0 & \delta \end{pmatrix} \quad (2.9)$$

where we defined the Rabi frequency  $\Omega_0 = -\mathbf{d} \cdot \mathcal{E}/\hbar$ . Through diagonalization of this Hamiltonian, we obtain the eigenstates of the system consisting of the atom dressed with the photons and including the interaction. We label these eigenstates dressed states and find them to be linear combination of the bare states

$$\begin{aligned} |1(N)\rangle &= \sin\theta |g, N + 1\rangle + \cos\theta |e, N\rangle \\ |2(N)\rangle &= \cos\theta |g, N + 1\rangle - \sin\theta |e, N\rangle \end{aligned} \quad (2.10)$$

where  $\tan 2\theta = -\Omega_0/\delta$ . The energy difference between the dressed states is given by the generalized Rabi frequency  $\Omega = \hbar\sqrt{\delta^2 + \Omega_0^2}$  as shown in Fig. 2.1 b). When we plot the energy of the states against the detuning (Fig. 2.1 c)) we find that level crossing of the bare states turns into an avoided crossing when we take the interactions into account by means of the dressed states. Far from resonance, the deviation from the dressed states to the bare states corresponds to the AC Stark effect.

## 2.2 Spin-1 system

Our experimental system, a  $^{87}\text{Rb}$  BEC, is generated in the electronic ground state and most of the experiments are carried out in the  $F = 1$  manifold which forms a spin-1 system. In order to describe the behavior and the dynamics of our system, we start by setting up a theoretical framework for the spin-1 system. First, we consider a single spin-1 particle before we extend our description towards an interacting ensemble in the many body limit.

### 2.2.1 Single particle description

In order to describe a spin-1 system we can extend the well known formalism of the spin-1/2 system. Instead of a two-level system we are dealing with a three-level system which is given in

our case by the three magnetic substates  $|m_F\rangle$  with  $m_F \in \{-1, 0, +1\}$  of the  $F = 1$  manifold. With those basis states, a pure single-particle state is given as

$$|\Psi\rangle = \sqrt{c_{+1}} e^{i\phi_{+1}} | +1\rangle + \sqrt{c_0} e^{i\phi_0} | 0\rangle + \sqrt{c_{-1}} e^{i\phi_{-1}} | -1\rangle \quad (2.11)$$

where the prefactors  $c_i$  give the probability of finding the particle in state  $|i\rangle$  and are normalized with  $\sum_i c_i = 1$ . Since the absolute value of the phases  $\phi_i$  cannot be measured, we neglect the overall phase and only consider the relative phases by

$$|\Psi\rangle = \begin{pmatrix} \sqrt{c_{+1}} e^{i\phi_L/2} \\ \sqrt{c_0} e^{i\phi_S} \\ \sqrt{c_{-1}} e^{-i\phi_L/2} \end{pmatrix} \quad (2.12)$$

where we used the vector notation. Here, the phase difference between the states  $|\pm 1\rangle$  is defined as the Larmor phase  $\phi_L = \phi_{+1} - \phi_{-1}$ , while  $\phi_S = \phi_0 - (\phi_{+1} + \phi_{-1})$  is defined as the spinor phase. The free parameters of the spin-1 particle, gives rise to a set of unitary transformations which are covered by the Lie group  $SU(3)$ . To parameterize the transformations we define a basis for the hermitian operators of the Lie algebra  $\mathfrak{su}(3)$ . One choice for such a basis is given by the set

$$\left\{ \hat{F}_x, \hat{F}_y, \hat{F}_z, \hat{Q}_{xz}, \hat{Q}_{yz}, \hat{Q}_{xy}, \hat{Q}_{xx}, \hat{Q}_{yy} \right\} \quad (2.13)$$

where the first three, defined in analogy to the spin-1/2 system, are the spin-1 dipole operators given as [7]

$$\hat{F}_x = \frac{1}{\sqrt{2}} \begin{pmatrix} 0 & 1 & 0 \\ 1 & 0 & 1 \\ 0 & 1 & 0 \end{pmatrix}, \quad \hat{F}_y = \frac{1}{\sqrt{2}} \begin{pmatrix} 0 & -i & 0 \\ i & 0 & -i \\ 0 & i & 0 \end{pmatrix}, \quad \hat{F}_z = \frac{1}{\sqrt{2}} \begin{pmatrix} 1 & 0 & 0 \\ 0 & 0 & 0 \\ 0 & 0 & -1 \end{pmatrix} \quad (2.14)$$

Contrary to a spin-1/2 particle, we require additional operators to fully specify the wavefunction, for which we choose the quadrupole operators defined as [8]

$$\hat{Q}_{ij} = \hat{F}_i \hat{F}_j + \hat{F}_j \hat{F}_i - \frac{4}{3} \delta_{ij} \mathbb{1}_3 \quad i, j \in \{x, y, z\} \quad (2.15)$$

where  $\delta_{ij}$  denotes the Kronecker delta. With the set of operators (2.13) we can decompose the density matrix of any state by [9]

$$\hat{\rho} = \frac{1}{3} \mathbb{1}_3 + \sum_i f_i \hat{F}_i + \sum_j q_j \hat{Q}_j \quad (2.16)$$

The operators (2.13) are the generators of  $SU(3)$  and can be used to describe any unitary transformation of a spin-1 state.

### 2.2.2 Many-body limit

In a single experimental realization we probe the spin dynamics of at least  $\sim 10^4$  interacting atoms. In order to describe this system, we have to extend the single particle spin-1 formalism to the many-body limit. As our system is a Bose-Einstein condensate of identical atoms, the particles are indistinguishable and the many-body state has to reflect this property by being symmetric under the exchange of any two particles. It is thus no longer practical to ask for the state of each individual particle, but rather one should determine by how many particles each state is occupied. This approach is realized in the second quantization formalism where the many-body basis state is given by the Fock state

$$|\psi\rangle = |N_{+1}, N_0, N_{-1}\rangle \quad (2.17)$$

where  $N_m$  is the number of atoms in the respective magnetic substate. In eq. (2.17) we applied the single-mode approximation, where we assume that all magnetic substates occupy the same spatial mode. We can express the set of spin-1 operators (2.13) in the second quantization formalism using the Jordan-Schwinger map [10]

$$\hat{O} = \left( \hat{a}_{+1}^\dagger, \hat{a}_0^\dagger, \hat{a}_{-1}^\dagger \right) \hat{O}_{1st} \begin{pmatrix} \hat{a}_{+1} \\ \hat{a}_0 \\ \hat{a}_{-1} \end{pmatrix} \quad (2.18)$$

where  $\hat{O}_{1st}$  denotes an operator in the matrix notation and  $\hat{a}_m^\dagger$  and  $\hat{a}_m$  are the creation and annihilation operators of the magnetic substate  $m$ . The number of atoms in the state  $m$  is given by the number operator

$$\hat{N}_m = \hat{a}_m^\dagger \hat{a}_m \quad (2.19)$$

In section 3.3 we will use this formalism to describe our spin-1 system, where we also will include the interactions between the atoms.

## 3 Experimental system

In this chapter a brief overview of the experimental platform, a spinor Bose-Einstein condensate (BEC) of  $^{87}\text{Rb}$ , is given. After describing the condensation process, we detail on the internal level structure of  $^{87}\text{Rb}$ . Then, we take a look at the interactions and how we control them experimentally, before presenting the typical mode of operation of the experiment.

### 3.1 BEC generation and trapping potential

The geometric setup and the BEC production is already described in plenty of previous theses [9] [11] [12], so we will only summarize the key elements here. The condensate is produced in ultra-high vacuum conditions with a sequence of cooling and trapping techniques. Each experimental run starts by confining  $^{87}\text{Rb}$  atoms in a magneto-optical trap (MOT). Following a short sub-Doppler cooling cycle, the atoms are transferred to a magnetic trap in the time-orbiting-potential (TOP) configuration where further cooling is achieved by evaporative cooling. Subsequently, the atoms are loaded into a optical dipole trap created by two far-red detuned (1030 nm) focused laser beams referred to as XDT and waveguide (WG). Here, further evaporative cooling is induced by reducing the power in the laser beams thereby letting the hotter atoms escape, leading to a BEC of up to  $\sim 10^5$  atoms. After the evaporation the XDT beam is ramped down, while the waveguides intensity is ramped up slightly leading to a very elongated dipole trap with trapping frequencies  $(\omega_{\parallel}, \omega_{\perp}) \approx 2\pi \times (1.6, 170)$  Hz. The geometric configuration of the dipole trap beams and the glass cell is sketched in Fig. 3.1 a). The cooling cycle takes around 37 s and yields the condensed  $^{87}\text{Rb}$  atoms in the  $(F, m_F) = (1, -1)$  hyperfine state, which is the starting point for all our experiments.

#### Trapping potential

In the optical dipole trap of the WG beam, the radial extension of the atomic cloud is small enough, such that typically no spin excitations emerge in this direction. Therefore, we investigate in the dynamics of a quasi-one-dimensional spin system. The atomic density, however, adjusts itself to the trapping potential and is hence inhomogeneous. This leads to a generally unwanted spatial dependency of the spin-spin interaction, since they are influenced by the density. To circumvent this, we confine the atoms to the central part of the dipole trap where the density only varies slightly. This is achieved by shining in two blue-detuned laser beams ( $\lambda \approx 760$  nm) symmetrically around the harmonic trap center, which generate a repulsive potential. The position of these beams is controlled with a setup of two acousto-optic deflectors (AODs) [13]. In these devices, a laser beam is deflected by a crystal, through which a sound wave is traveling perpendicular to the beam's direction of propagation. The acoustic frequency determines the deflection angle and thus enables spatially controlling the laser beam.

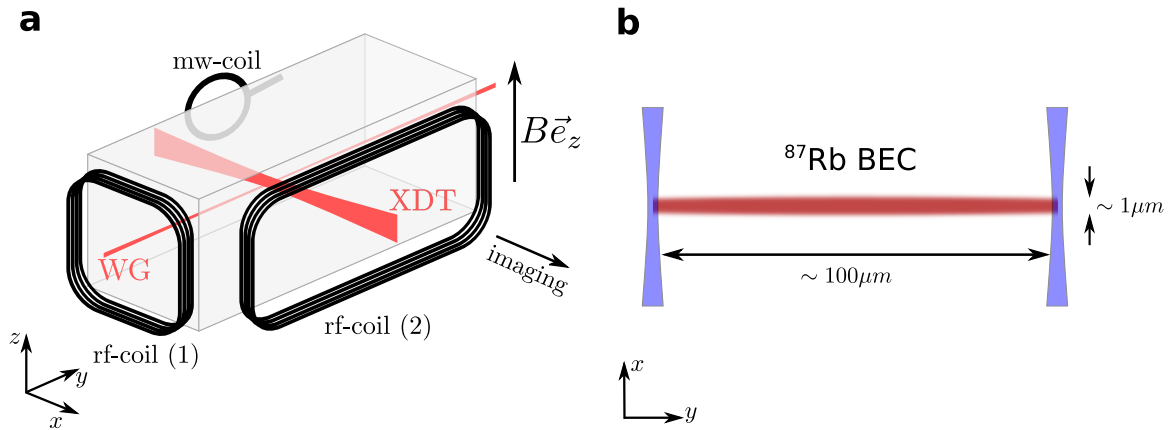


**Figure 3.1 a) Experimental configuration.** Sketch of the glass cell in which the BEC is generated under ultra-high vacuum conditions. In the crossed optical dipole trap consisting of the XDT beam and the WG beam, condensation is achieved by evaporative cooling. Also shown are the two coils used to drive radio-frequency transition and the microwave antenna. Fig. a) is adapted from [9]. **b) Box-like trapping potential.** After adiabatically turning off the XDT beam, the atomic cloud expands into the elongated quasi-one-dimensional trapping potential of the WG beam. In order to achieve an atomic density profile along the cloud which is as homogeneous as possible, the trap is further confined with blue detuned laser beams on each side. The resulting atomic density profile resembles a one-dimensional box, i.e. it is quite homogeneous with steep edges. The width of the box can be set to any desired value, as we have full control over the location of the two beams.

With one AOD regulating the deflection in horizontal direction and a second AOD regulating the vertical deflection, we have full spatial control over the laser beam and can steer it to overlap with the atomic cloud at any point. By constraining the quasi-one-dimensional trap on both sides as illustrated in Fig. 3.1 b), we generate a box-like trapping potential. In the cooling sequence, when the XDT beam from the crossed dipole trap is ramped down after the final evaporative cooling cycle, the atomic cloud expands into this harmonic potential of the WG constrained by the blue detuned beams.

Furthermore, an important feature for modifying the spatial structure of our system is given by the possibility to generate an optical lattice potential [12]. For this, two laser beams are crossed under a shallow angle which forms a one-dimensional lattice in the longitudinal direction of the cloud. The angle and the wavelength of the laser beams determine the spacing of the lattice wells [14]. As it is energetically favorable, the atoms are forced towards the minima of the lattice potential and hence the homogeneous atomic cloud is divided into many small clouds, which are separated from each other. In the current setting, the single large BEC confined in the box-like potential is transformed with the lattice into  $\sim 20$  independent small BEC's.

## 3.2 Level structure

The  $^{87}\text{Rb}$  atoms are trapped in their electronic ground state  $5^2S_{1/2}$ , where the coupling between the nuclear spin  $I = 3/2$  and the valence electron's spin  $S = 1/2$  results in the emergence of two hyperfine manifolds  $F = 1, 2$ . The frequency splitting between these hyperfine manifolds

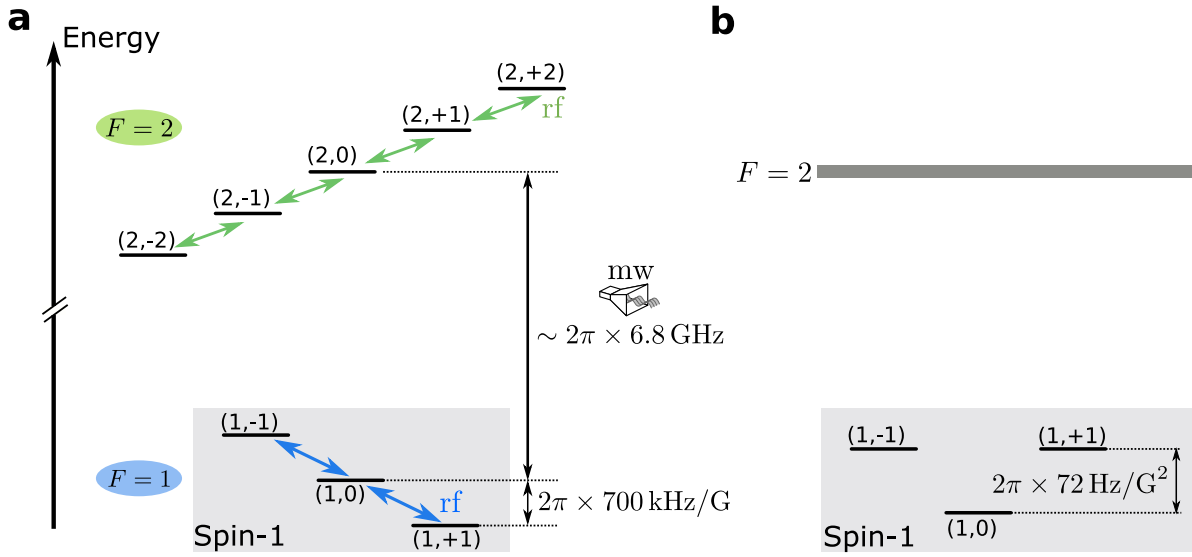


**Figure 3.2** Level structure of  $^{87}\text{Rb}$  in its electronic ground state. **a)** The two hyperfine manifolds  $F = 1$  and  $F = 2$  with a frequency splitting of  $\sim 2\pi \times 6.8$  GHz are shown. The magnetic substates are shifted due to the linear Zeeman effect. **b)** When transforming into the rotating frame of the Larmor frequency of  $F = 1$ , the linear Zeeman effect vanishes and the quadratic shift is revealed where the  $(1,0)$  level is shifted relative to the  $(1,\pm 1)$  levels by  $\sim 2\pi \times 72$  Hz/G $^2$ .

is  $\omega_{hfs} = 2\pi \cdot 6.835$  GHz [15]. During the experiments, a magnetic bias field of  $B = 0.894$  G is applied along the  $z$ -direction which we also define as the quantization axis. This lifts the degeneracy of the  $2F + 1$  magnetic sublevels of each manifold, as their energy is shifted due to the Zeeman effect. Throughout this thesis we will use the notation  $(F, m_F)$  to refer to the magnetic substates. As given in [9], the linear and the quadratic shifts are

$$E_z = g_{1,F} m_F \hbar B + g_{2,F} (4 - m_F^2) \hbar B^2 \quad (3.1)$$

where  $\hbar$  is the reduced Planck constant and the first- and second-order g-factors are

$$g_{1,F} \approx \begin{cases} -2\pi \times 700 \text{ kHz/G} & \text{for } F = 1 \\ 2\pi \times 702 \text{ kHz/G} & \text{for } F = 2 \end{cases} \quad (3.2)$$

$$g_{2,F} \approx \begin{cases} -2\pi \times 72 \text{ Hz/G}^2 & \text{for } F = 1 \\ 2\pi \times 72 \text{ Hz/G}^2 & \text{for } F = 2 \end{cases}$$

Interestingly, the magnitude of the Zeeman shift is almost the same for both hyperfine manifolds, however the g-factors have a different sign, leading to the level structure shown in Fig. 3.2 a). In  $F = 1$  the energy splitting of the linear Zeeman effect results in the Larmor precession of the spin around the  $z$ -axis with the frequency  $\omega_L = 2\pi \times g_{1,1} B$ .

Looking at the g-factors, it is clear that at the employed magnetic field strength the quadratic Zeeman effect is significantly smaller. A transformation into the frame co-rotating with the Larmor frequency though, removes the linear shift and presents the effect of the quadratic shift shown in Fig. 3.2 b). According to eq. (3.1), the second order term shifts the zero mode  $(1,0)$  relative to the  $m_F = \pm 1$  states by  $q_B = -2\pi \times 72 \text{ Hz/G}^2 \times B^2$ , which results in a spinor phase evolution. The  $F = 1$  hyperfine manifold gives access to a spin-1 system, in which most of

our experiments are conducted. Here and throughout this thesis, we will refer to the  $m_F = \pm 1$  states as side modes.

### 3.3 Interactions in a spin-1 system

In the following we briefly review the theoretical description for a many-body system composed of interacting spin-1 particles. We describe each magnetic sublevel with a bosonic field operator, which we combine in the vector

$$\hat{\Psi}(\mathbf{r}) = \begin{pmatrix} \hat{\Psi}_{+1}(\mathbf{r}) \\ \hat{\Psi}_0(\mathbf{r}) \\ \hat{\Psi}_{-1}(\mathbf{r}) \end{pmatrix} \quad (3.3)$$

We expand the field operators with a set of basis functions  $\phi_{mi}(\mathbf{r})$  as

$$\hat{\Psi}_m(\mathbf{r}) = \sum_i \phi_{mi}(\mathbf{r}) \hat{a}_{mi} \quad (3.4)$$

$\stackrel{SMA}{=} \phi_C(\mathbf{r}) \hat{a}_m$

where  $\hat{a}_{mi}$  is the annihilation operator for the magnetic quantum number  $m$  and the spatial mode  $i$ . For a homogeneous Bose-Einstein condensate, we further can apply the single-mode approximation (SMA) where we assume that all particles occupy the same spatial mode  $\phi_C(\mathbf{r})$ . The Hamiltonian describing our system, can be divided into three parts

$$\hat{\mathcal{H}} = \int d\mathbf{r} \left( \hat{\mathcal{H}}_0 + \hat{\mathcal{H}}_B + \hat{\mathcal{H}}_{\text{int}} \right) \quad (3.5)$$

where the single particle term  $\hat{\mathcal{H}}_0$  describes the kinetic energy and the potential energy due to the confinement in the optical trap

$$\hat{\mathcal{H}}_0 = \hat{\Psi}^\dagger(\mathbf{r}) \left( \frac{\hbar^2 \nabla^2}{2M} + V_{\text{trap}}(\mathbf{r}) \right) \hat{\Psi}(\mathbf{r}) \quad (3.6)$$

where  $\hbar$  is the reduced Planck constant and  $M$  the atomic mass. Since the experiments are carried out in the presence of a magnetic bias field, we include the energy shifts of the magnetic substates due to the Zeeman effect with

$$\hat{\mathcal{H}}_B = \hbar p_B \hat{F}_z(\mathbf{r}) + \hbar q_B \left( \hat{N}_{+1}(\mathbf{r}) + \hat{N}_{-1}(\mathbf{r}) \right) \quad (3.7)$$

where  $p_B = g_{1,1}B$  and  $q_B = -g_{2,1}B^2$  give the linear and the quadratic shift respectively (compare to eq.(3.1)).

## Interactions

The interesting dynamics that we want to study are induced by the interactions between the atoms. For alkali atoms in the electronic ground state long-range interactions, like the dipole-dipole interaction, are very weak and can be neglected. Short-range interactions on the other

hand, are sufficiently described with only two-body scattering events, as three or more-body scattering is highly unlikely in our very dilute system. Further, in the ultracold gas s-wave scattering is by far the dominant scattering channel.

Due to the symmetry of the many-body wave function under the exchange of two particles and due to the conservation of the total spin in binary collisions, only the two spin channels with  $\mathcal{F} = \{0, 2\}$  are allowed, where  $\mathcal{F}$  is the total spin of the two interacting particles. Following the derivation in [16], this results in the interaction Hamiltonian

$$\hat{\mathcal{H}}_{\text{int}} = \frac{c_0 \chi}{2} : \hat{N}^2(\mathbf{r}) : + \frac{c_1 \chi}{2} : \hat{\mathbf{F}}^2(\mathbf{r}) : \quad (3.8)$$

where  $::$  denotes normal ordering,  $\hat{N} = \sum_m \hat{N}_m = \sum_m \hat{a}_m^\dagger \hat{a}_m$  is the total density operator and  $\hat{\mathbf{F}} = (\hat{F}_x, \hat{F}_y, \hat{F}_z)^T$  the vector of the spin-dipole operators. Here,  $\chi = \int d\mathbf{r} \phi_0^2 \phi_{+1}^* \phi_{-1}^*$  describes the mode overlap. Due to the single mode approximation in eq.(3.4), all states occupy the same spatial mode and we obtain  $\chi = \int d\mathbf{r} |\phi_C(\mathbf{r})|^4$ . The first term in 3.8 describes an overall energy shift due to interactions depending on the atomic density, while the second part is spin dependent. The coupling constants of these two interactions are

$$\begin{aligned} c_0 &= \frac{4\pi\hbar^2}{M} \frac{a_0 + 2a_2}{3} \\ c_1 &= \frac{4\pi\hbar^2}{M} \frac{a_2 - a_0}{3} \end{aligned} \quad (3.9)$$

where  $a_0$  and  $a_2$  are the s-wave scattering lengths of the corresponding spin channels and their values can be found in [16]. It is however important to note that in the  $F = 1$  manifold of  $^{87}\text{Rb}$  the coupling constant  $c_1$  is negative. Thus, it is energetically favorable for the spin of all atoms to align resulting in the ferromagnetic characteristic of the interactions in our system. To get a better understanding of the spin-spin interactions, we plug the operators in second quantization in the spin dependent part of eq. (3.8) and expand it to [9]

$$\begin{aligned} \hat{\mathcal{H}}_{\text{spin}} &= \frac{\tilde{c}_1}{2} : \left( \hat{F}_x \hat{F}_x + \hat{F}_y \hat{F}_y + \hat{F}_z \hat{F}_z \right) : \\ &= \tilde{c}_1 \hat{N} \\ &\quad + \tilde{c}_1 \left( \hat{N}_0 - \frac{1}{2} \right) \left( \hat{N}_{+1} + \hat{N}_{-1} \right) \\ &\quad + \frac{\tilde{c}_1}{2} : \left( \hat{N}_{+1} - \hat{N}_{-1} \right)^2 : \\ &\quad + \tilde{c}_1 \left( \hat{a}_0^\dagger \hat{a}_0^\dagger \hat{a}_{+1} \hat{a}_{-1} + \hat{a}_{+1}^\dagger \hat{a}_{-1}^\dagger \hat{a}_0 \hat{a}_0 \right) \end{aligned} \quad (3.10)$$

where we used the modified coupling constant  $\tilde{c}_1 = c_1 \chi$ . With the spin Hamiltonian written out in this formulation, it is easy to identify the physical meaning of the different parts. While the first term yields an overall energy shift, the second one shifts the energy of the (1,0) state relative to the side modes. The third line shows that an imbalance in the population of the side modes is energetically favored. But since the  $z$ -component of the spin is conserved during

collisions, the imbalance in the side mode population cannot be altered by the interactions. All experiments discussed here have no magnetization in  $z$ -direction when integrating over the entire system, so this term vanishes. The last term is essential for the internal dynamics as it gives rise to so called spin-changing collisions. These are scattering events where two atoms, initially occupying the state  $(1,0)$ , are transformed into an atom pair where one particle is in the  $m_F = +1$  and the other one in the  $m_F = -1$  state. This process also occurs the other way around and generally leads to highly entangled states.

Now, we have specified the different parts in the Hamiltonian (3.5). We are, however, especially interested in the internal spin dynamics, hence we will identify the relevant contributions. For this purpose, global energy shifts and finite magnetization effects can be neglected. As collisions fulfill conservation of the spin's  $z$ -component, the linear Zeeman splitting is also irrelevant. In the case of spin-changing collisions, where a pair of atoms in  $(1,0)$  is transferred into the side modes  $(1,\pm 1)$ , one can notice that the initial and final pair states have the same energy according to the first order Zeeman splitting. The quadratic Zeeman effect, on the other hand, shifts in particular the energy of the side modes relative to the  $m_F = 0$  level. As a result, the internal dynamics are described by the Hamiltonian

$$\hat{\mathcal{H}} = q \left( \hat{N}_{+1}(\mathbf{r}) + \hat{N}_{-1}(\mathbf{r}) \right) + \frac{\tilde{c}_1}{2} : \left( \hat{F}_x^2 + \hat{F}_y^2 + \hat{F}_z^2 \right) : \quad (3.11)$$

Besides the ferromagnetic behavior, the energy splitting between the  $m_F = 0$  state and the side modes plays an important role for the internal behavior. In the experiment we tune this splitting, given by  $q$ , to obtain a control parameter over the internal dynamics.

## 3.4 Internal control

High control over the internal state of the atoms is essential throughout the experiment. In order to study the dynamics of our spin-1 BEC, it is particularly necessary to reliably prepare an initial state, induce spin-changing collisions and readout different observables. An important tool for achieving this is applying linearly oscillating magnetic fields which couple distinct hyperfine states of the level structure where microwave (mw) frequencies couple states of different manifolds and radio-frequencies (rf) couple the substates within a manifold. These fields are generated with a microwave coil and two radio frequency coils respectively which are installed directly next to the glass cell as sketched in Fig. 3.1.

### Microwave and radio-frequency pulses

The mw pulses are used to drive transitions between the two hyperfine manifolds with the purpose of transferring atoms between two substates. This can be described as a coupled two-level system (see Sec. 2.1), where the population will carry out Rabi oscillations. By precisely controlling the duration of a pulse, we can determine the exact amount of the population that will be transferred. With the Rabi frequency typically on the order of a few kHz, a total inversion of the population in form of a  $\pi$ -pulse takes a few hundred microseconds. Since the energy splitting of the magnetic substates is nearly the same in both manifolds, one has

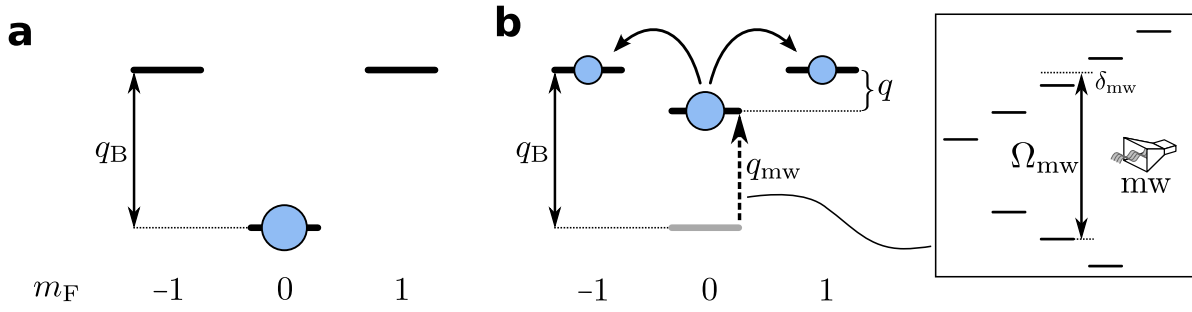


**Figure 3.3 Microwave dressing.** **a)** The quadratic Zeeman shift  $q_B$  gives the relevant level structure for the internal spin dynamics. At the employed bias field, however,  $q_B$  is way larger than the interaction energy of the spin-changing collisions and they are not resonant. **b)** Microwave dressing allows to tune the splitting to the effective value  $q$ , by off-resonantly coupling to the  $(1,0) \leftrightarrow (2,0)$  transition. Figure adapted from [9].

to be careful not to accidentally drive multiple transitions simultaneously. For instance when driving the transition  $(1,0) \leftrightarrow (2,1)$  one automatically also couples  $(1,1) \leftrightarrow (2,0)$ , due to the very similar transition frequencies. Further, the selection rules restrict us to mw transitions with a change in the magnetic quantum number of  $\Delta m_F = m_2 - m_1 = \{0, \pm 1\}$ . The microwave setup is discussed in more detail in Ch. 4.

The rf pulses couple all states within a manifold to each other. For the three sublevels in  $F = 1$ , this coupling leads to a Rabi oscillation which can be interpreted as a spin rotation on the spin-1 sphere. This process is described in detail in [9] [17]. Most importantly, however, this allows us to map different operators onto the quantization axis.

## Microwave dressing

In Sec. 3.3 we discussed the interactions in our spin-1 system and found that the internal spin dynamics are determined by eq. (3.11), where the energy difference between the  $(1,0)$  state and the side modes, given by  $q$ , is an important parameter. Intuitively this makes sense, when we think of the spin-changing collisions, where two atoms initially occupying the  $m_F = 0$  state are transferred to a final state where one atom is in the magnetic sublevel with  $m_F = -1$  and the other one is in  $m_F = +1$ . The energy difference between the initial and the final state depends on  $q$  and consequently this parameter determines whether the spin mixing process is energetically favorable or not. At the typically applied magnetic field strength, the quadratic Zeeman effect has an extent of  $q_B \approx 2\pi \times 58$  Hz. The coupling strength of the spin-spin interactions, on the other hand, is only on the order of  $2\pi \times 2$  Hz. In this setting (see Fig. 3.3 a)) spin-changing collisions are strongly suppressed and do not occur.

In order to enable and control the spin dynamics we need to adjust the energy mismatch between the initial and the final state of the atom pair in the spin-changing collisions. For this purpose, we employ so-called microwave dressing [18]. In this technique, an off-resonant microwave field is used to couple the states  $(1,0) \leftrightarrow (2,0)$ . This induces an energy shift of the  $(1,0)$  state due to the ac-Stark effect which is given by

$$\Delta E = \frac{\hbar \Omega_{\text{mw}}^2}{4\delta_{\text{mw}}} \quad (3.12)$$

where  $\delta_{\text{mw}} = \omega_{\text{hfs}} - \omega_{\text{mw}}$  is the detuning of the microwave frequency to the transition frequency of the hyperfine splitting. In the resonant case, the Rabi frequency is usually on the order of  $\Omega_{\text{mw}} \approx 2\pi \cdot 7.7 \text{ kHz}$ . To shift the energy of the (1,0) state, we employ mw dressing with a detuning of about  $\delta_{\text{mw}} \approx 2\pi \cdot 150 \text{ kHz}$ , so the probability of transferring atoms to the (2,0) state is only  $\eta = \Omega_{\text{mw}}^2 / (\Omega_{\text{mw}}^2 + \delta_{\text{mw}}^2) < 0.3\%$ . The microwave dressing leads to an effective frequency splitting given by

$$q = q_B + q_{\text{mw}} \quad \text{with } q_{\text{mw}} = \frac{\Delta E}{\hbar} = \frac{\Omega_{\text{mw}}^2}{4\delta_{\text{mw}}} \quad (3.13)$$

We can tune  $q$  by changing either the Rabi frequency or the detuning, whereof we typically choose the latter in our experiments. In fact, we have high control over the microwave fields, making  $q$  the optimal experimental parameter for controlling the internal dynamics. In particular, we can quench the system by suddenly switching on the dressing field or by changing the detuning.

Due to the multilevel structure, there is also off-resonant coupling to other magnetic substates, so the true value of  $q$  is slightly different. For the employed bias field, other transitions are at least off-resonant by  $\sim 2\pi \times 450 \text{ kHz}$  and are thus neglected in the calculations here. In the experiment, however, it is crucial to set the exact value correctly, which is why we adjust  $q$  relative to a spectroscopy measurement.

### 3.5 Mean-field phase diagram

To investigate in the dynamical behavior of our spin-1 system, it is beneficial to know how the ground state of our system is characterized, especially in dependence of the experimental control parameter  $q$ . In the following we will determine this in the mean-field description, where we also can construct the corresponding phase diagram. Here we will merely state some results, while a detailed derivation for obtaining a mean-field picture is given in [16].

In mean-field theory, the field operators are replaced by their expectation value. Hence, we evaluate the expectation value of the Hamiltonian (3.11) to receive an energy functional for the internal dynamics of the system. Therefore, we consider a uniform system with a fixed number density  $n = \langle \hat{N}(\mathbf{r}) \rangle$  where we define a normalized spinor  $\xi_m = \Psi_m / \sqrt{n}$  and the spin expectation value per particle  $\mathbf{f} = 1/n \langle \mathbf{F} \rangle$ . The energy per particle is then given by the energy functional

$$\epsilon = \sum_i q m^2 |\xi_m|^2 + \frac{1}{2} c_1 n |\mathbf{f}|^2 \quad (3.14)$$

where the spin-spin interaction constant is defined in eq. (3.9) and describes the ferromagnetic behavior ( $c_1 > 0$ ). The ground state can be identified as the state that minimizes the energy functional. For the parameter space  $(q, c_1)$  this yields different ground states shown in the phase diagram in Fig. 3.4. The ferromagnetic regime ( $c_1 < 0$ ), in which the  $F = 1$  manifold

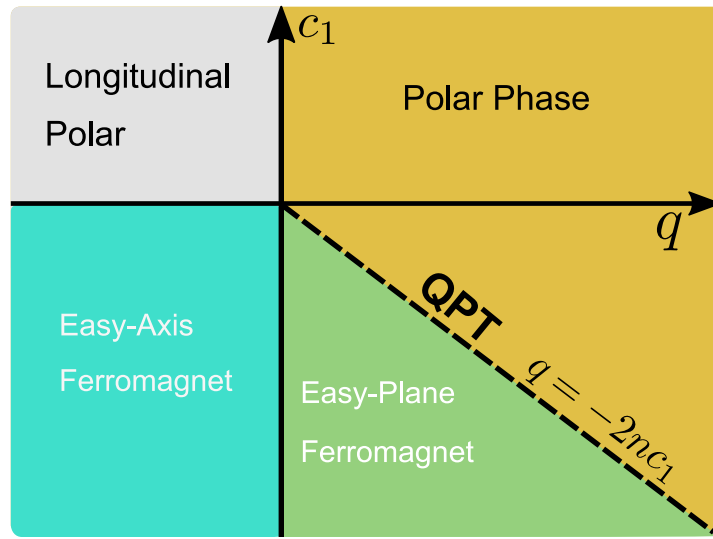


**Figure 3.4 Mean-field phase diagram.** In dependence of the parameters  $q$  and  $c_1$ , the spin-1 system exhibits different mean-field ground states leading to different phases. Figure adapted from [11].

of  $^{87}\text{Rb}$  falls, exhibits three ground states depending on  $q$ . The different phases intuitively make sense when considering that  $q$  is the energy splitting between  $(1,0)$  and the side modes. For large  $q$ , the  $(1,0)$  state is energetically considerably lower than the side modes and the ground state in this case is therefore given by a global occupation of  $m_F = 0$ , which is called the polar state and results in  $\xi = (0, 1, 0)$ . For  $q$  on the order of the spin interaction, one finds the easy-plane ferromagnetic phase instead, where the ground state is given by the spinor

$$\xi = (\sin \theta / \sqrt{2}, \cos \theta, \sin \theta / \sqrt{2})^T \quad \text{where} \quad \sin \theta = \sqrt{\frac{1}{2} + \frac{q}{4nc_1}} \quad (3.15)$$

This describes a magnetization in the transversal plane where all directions in the plane are equally likely. In each realization, this symmetry around the  $z$ -axis is spontaneously broken as one direction is chosen randomly. Finally, for  $q < 0$  the ground state is either  $\xi = (1, 0, 0)$  or  $\xi = (0, 0, 1)$  whereof both are fully polarized and require finite magnetization.

## 3.6 Typical experimental run

Each experimental run follows a similar routine consisting out of the following steps

1. Initial state preparation
2. Time evolution
3. Readout

The cooling cycle results in a condensate with all atoms occupying the  $(1,-1)$  level. As starting point of our experiment a well-defined initial state is required. This is accomplished by controlling the internal state with the mw and rf pulses. We will outline this process for one

particular initial condition, namely the polar state where all atoms are in  $(1,0)$ . To prepare this, two mw  $\pi$ -pulses are applied where the first one drives the transition  $(1,-1) \leftrightarrow (2,0)$  thereby transferring all atoms into  $(2,0)$  and the second one drives  $(1,0) \leftrightarrow (2,0)$  which already results in the polar state. To get rid of any remaining population in the states  $(1,\pm 1)$  we shortly apply a strong magnetic field gradient to remove these atoms from the trap.

Now, we usually want to initiate some interesting dynamics. This can be achieved by quenching the system to a different  $q$  by suddenly turning on the mw dressing and thereby driving the system over a phase transition. Another possibility to initiate dynamical behavior is to create topological excitations by locally generating pairs of three-component solitons [19]. Subsequently, the dynamics may develop for a desired duration which corresponds to the time evolution under the Hamiltonian (3.5).

We measure the state obtained after the time evolution with hyperfine selective absorption imaging. We can also choose which observables we measure, by applying rf spin rotations prior to the readout. The measurement process is however destructive, as the imaging light strongly heats the atomic cloud and eliminates the condensate. Thus, the ability to repeat an experimental run many times without a change of any parameters is highly important.

### 3.7 Readout

The final state of the condensate is measured by high intensity absorption imaging [20]. This is accomplished by shining light resonant with the transition to an excited electronic state ( $D_2$  line) onto the atoms. The light is partly scattered and consequently has reduced intensity behind the cloud, which is imaged with a CCD camera and allows to determine the spatially resolved atomic densities. In fact, we apply two  $15 \mu\text{s}$  light pulses where the first images the  $F = 2$  and the second one the  $F = 1$  hyperfine manifold. Prior to that, we turn off the trapping beams and use a Stern-Gerlach magnetic field gradient in  $z$ -direction, which physically moves the atoms according to their  $m_F$  state such that the magnetic sublevels can be distinguished on the image. The readout method is thus capable of measuring the spatially resolved density profiles  $N_i(y)$  of all eight magnetic substates. A typical absorption image is shown in Fig. 3.5.

Without applying any additional rf or mw pulses prior to the readout, the  $F = 2$  manifold will be unoccupied and from the  $F = 1$  states we can directly calculate the  $z$ -component of the spin along the cloud with

$$F_z(y) = \frac{N_{+1}(y) - N_{-1}(y)}{N_{tot}(y)} \quad (3.16)$$

where  $N_{tot}(y)$  is the total atom number and  $F_z(y)$  is the spin projection in  $z$ -direction along the cloud in a single realization. Due to the fixed geometric setup, only projections onto the  $z$ -direction can be measured. Thanks to the high control over the internal state of the condensate though, it is possible to map other spin projections onto the  $z$ -axis.

The simplest option is imaging one transversal spin projection. This is implemented with a resonant rf  $\pi/2$ -pulse which rotates one transversal spin projection (i.e.  $F_x$  or  $F_y$ ) onto the  $z$ -axis where it can be measured and determined just like the  $F_z(y)$  in eq. (3.16). Furthermore, we can also employ a more advanced readout protocol, where multiple spin observables are detected simultaneously [21]. For this, the initially empty  $F = 2$  hyperfine levels are used

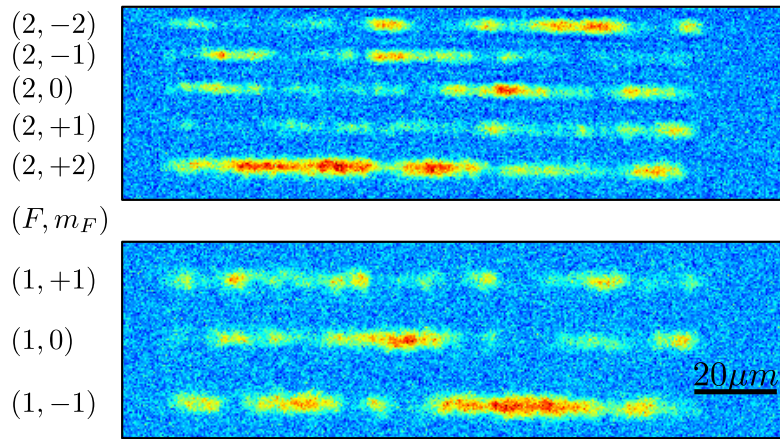


**Figure 3.5 Absorption image.** The images show the spatially resolved atomic densities in the different magnetic sublevels measured in a single realization. Prior to the readout, a magnetic field gradient is applied to spatially separate the magnetic sublevels. The upper absorption image shows the  $F = 2$  manifold which is imaged separately from the  $F = 1$  image shown below. In the particular single realization shown here, the initially empty  $F = 2$  manifold is utilized to measure multiple observables simultaneously. Therefore, a part of the population is transferred to  $F = 2$  using mw pulses and the internal state is rotated with rf pulses.

as auxiliary states for the readout. Prior to the imaging pulses, we transfer a fraction of the populations into the  $F = 2$  manifold where we can readout different spin-1 observables. With the five additional substates we even can measure noncommuting observables like  $F_x, F_y$  and  $F_z$  simultaneously. For the realization in Fig. 3.5 these three observables are measured simultaneously, such that all 8 sublevels are occupied.

## 4 Microwave stabilization

### 4.1 Motivation

In order to investigate in the dynamics of a spin-1 BEC, high control over its spatial shape and over the internal state of the atoms is necessary. The internal dynamics are, among other techniques, controlled by the use of microwave magnetic fields which drive transitions in between the hyperfine manifolds of the electronic ground state and are used to control and initiate dynamics, as they can tune the effective quadratic Zeeman shift  $q$  through mw dressing. Due to the probabilistic nature of quantum mechanics, it is of great importance, that all parameters which influence the system are stable over long time scales, because we have to measure many single realizations to draw conclusions about the dynamics.

To achieve operations under long-term steady circumstances (days, preferably even weeks), many parts of the experiment are actively stabilized. Especially, a robust setting of the experimental control parameter  $q$  is important, which depends on the magnetic bias field and on the power and frequency of the mw dressing (see eq. 3.13). The magnetic field is measured with a magnetic flux gate sensor to reduce the fluctuations to less than 0.1 mG. Additionally, we conduct a Ramsey sequence once every hour to compensate for drifts of the magnetic field. While the microwave frequency is highly stable, the microwave power on the other hand shows larger fluctuations and drifts. This directly influences the Rabi frequency and thus  $q$ . When we operate at  $q \approx 0$  a change in the Rabi frequency of  $2\pi \times 50$  Hz shifts  $q$  by  $2\pi \times 1$  Hz which already is a significant change, when we consider that the width of the easy-plane ferromagnetic phase is only a few Hz. This change corresponds to a relative stability of  $q$  of  $\sim 17 \cdot 10^{-3}$ . To prevent such changes in  $q$ , we aim for a significantly better microwave power stability. For this reason we employ an stabilization technique for the microwave power. The setup applied for this purpose and its performance are discussed in detail in this chapter.

### 4.2 Microwave system

The experimental system for generating and controlling microwave signals, to which the ultracold atoms are exposed to, is shown in Fig. 4.1. The magnetic fields oscillating at a microwave frequency of  $\sim 2\pi \times 6.8$  GHz couple the  $F = 1$  and  $F = 2$  hyperfine manifolds, which enables us to carry out two important processes. The first is the transfer of atoms between magnetic substates of the hyperfine manifolds by applying short pulses, whose duration has to be precisely adjustable, as this determines the fraction of the population being transferred. The second function is tuning the experimental control parameter  $q$  through microwave dressing which, as illustrated in section 4.1, requires a highly stable microwave power in order to robustly set  $q$ . The microwave setup is designed to fulfill these two puposes.

The employed system consists of two microwave synthesizers for generating a signal which passes through a series of amplifiers, attenuators and other rf-components before reaching the antenna located directly next to the glass cell. The antenna is a single loop of the solid copper core of the coaxial cable bent to a circle of  $\sim 14$ mm diameter. In order to use two synthesizers with only one antenna we have to merge their signal paths, which is done by a combiner, and forward the resulting signal to the antenna. It is however not intended to use both microwave generators at the same time and the combiner merely allows us to use either one of the two without rewiring. The synthesizers are connected to the experimental control system where the frequency and power level of the output is set. For our purposes a robust frequency is crucial and hence the synthesizers are frequency stabilized to a 10 MHz reference from an GPS disciplined ovenized quartz oscillator. We will now take a closer look at the generation of the short pulses.

## Pulse generation

During a typical experimental sequence several pulses are necessary to transfer the population to specific magnetic substates, mostly used for the initial state preparation and for the readout. As pulses with different transition frequencies have to be generated sequentially with as little time in between them as technically feasible, the microwave generator with a frequency switching time of  $\sim 7$  ms is too slow for our purposes.

Therefore, we operate the synthesizer on a fixed carrier frequency and the fine-tuning is achieved with an IQ mixer, where the in-phase and quadrature components of the input signal can be modulated separately. To do so, we use the two channels from an Keysight 33612A 80 MHz arbitrary waveform generator (AWG). The AWG has a sufficient bandwidth to drive all transitions and furthermore exhibits a high sampling rate of 660 MSa/s allowing very fast switching of the frequency and precise setting of the pulse duration. To further ensure that no unwanted signal gets through, a switch is located behind the mixer which only is closed during the pulse sequence. The components used for the pulse generation are shown in the green shaded box in Fig. 4.1. We utilize the signal of "MW 1" as carrier for the pulse generation before we combine the signal path with the one from "MW 2". In order to obtain sufficient power, we amplify the output signal of the combiner before we send it to the antenna.

### 4.2.1 Power stabilization

To achieve the required high stability of the power level of the microwave signal, we employ an external control loop (red shaded box in Fig. 4.1). This generally works by branching off a small portion of the signal in front of the antenna, measuring its power and comparing it to the desired value (set point). Knowing the deviation from the set point, we can compensate for it by adjusting the setting of a variable attenuator (PIN modulator) and thereby controlling the microwave power with this feedback mechanism. In the following, we will discuss the components of the stabilization loop in more detail:

**Detector:** As power detector we use the HP 423B, a low-barrier Schottky diode covering the frequency range between 10 MHz and 12.4 GHz. The input for the feedback loop is taken from

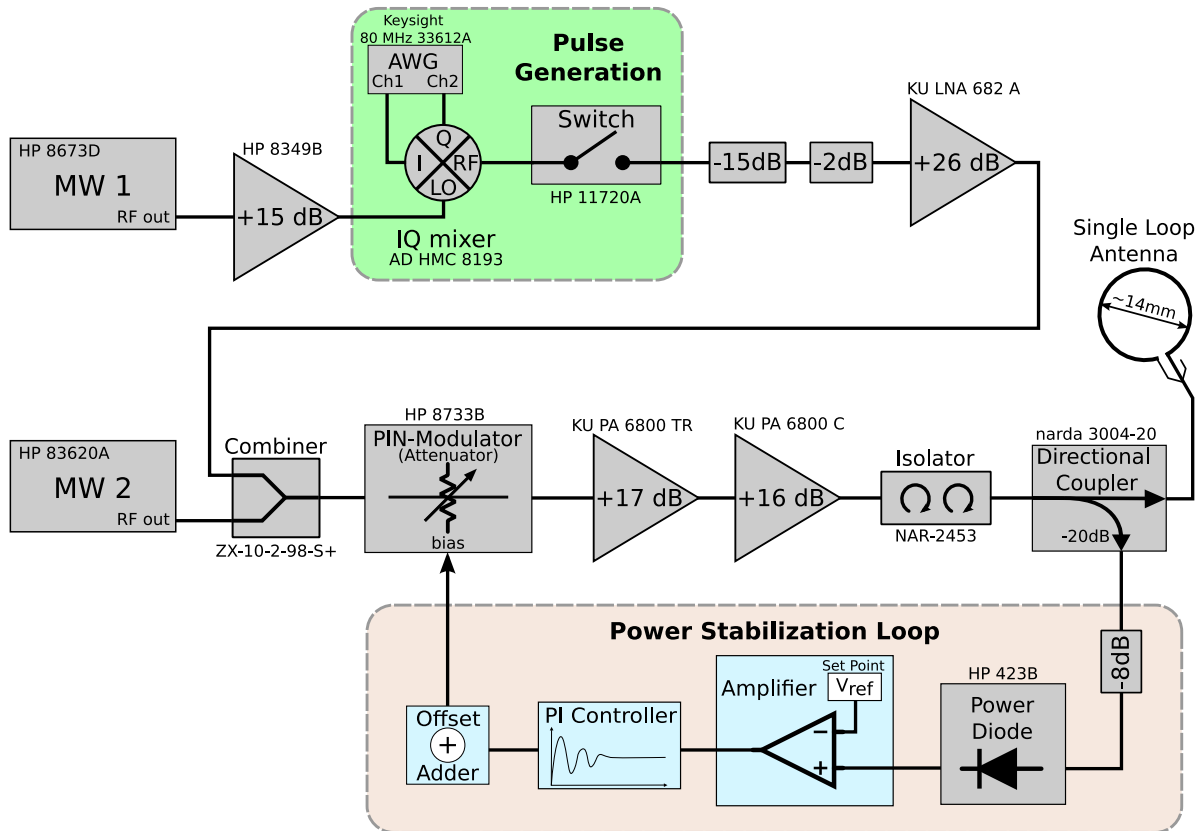


**Figure 4.1 Block circuit diagram of the microwave system.** Either one of the two microwave synthesizers can be used to generate a signal that is amplified and forwarded to a single loop antenna next to the glass cell. Before the two signal paths are combined, we mix the output of MW 1 at an IQ mixer with two sine signals provided by an AWG. This part, shown in the green shaded box, is used to generate short pulses of precise duration and it allows for very fast switching of the frequency. The signal path is then combined with MW 2 and subsequently passes through two amplifiers such that enough power reaches the antenna. In front of the antenna we utilize a directional coupler to take out a small part of the signal and use it as input for a control loop, which is responsible for actively stabilizing the power level. There, the current power level is measured with a power diode and compared to a set point. A PI-controller corrects the deviation to the set point by adjusting the attenuation of the PIN-modulator.

the signal proceeding to the antenna, where we branch off  $\sim 1\%$  with a directional coupler. This signal is further reduced in its power with an 8 dBm attenuator before being applied as input for the detector. In doing so we also ensure that the input power does not exceed the maximum of 23 dBm ( $\approx 200$  mW). The diode converts the mw signal oscillating at  $\sim 6.8$  GHz into a DC voltage proportional to the input power. The detector is particularly chosen due to its low noise level which is essential for reaching high stability. The power level on which we want to stabilize our setup results in an power diode output of  $\sim 200$  mV.

**Amplification:** The set point of our stabilization loop is given by the  $\sim 200$  mV on which we want the output of the detector to be. We thus try to minimize the deviation of the actual detector output to the set point. Accomplishing a high stability of  $10^{-4}$  would mean that on our 200 mV signal we get fluctuations with a standard deviation of only 20  $\mu$ V. This is a very weak error signal and it is necessary to amplify it, so that the signal to noise ratio is increased. For this purpose, we amplify the deviation from the set point with the precision instrumentation amplifier AD524. This integrated circuit amplifies the voltage difference between its two inputs by a factor of  $G = 1000$ . The output signal generated by the power diode serves as one of the inputs while the other one is the set point of the control loop and is given by a voltage reference (AD588) tuned to 200 mV. Then, the resulting output will be the amplified deviation from the set point, giving us exactly the quantity that we want to minimize in order to stabilize the microwave power. The complete electronic circuit with all components is given in Fig. A.1.

Since our goal is to reach a high level of stability, it is important to remember that all of the used components are not ideal and introduce additional noise sources. This includes of course the power diode itself, but also the the amplifier noise as well as fluctuations of the voltage reference are critical as they are strongly amplified and can not be filtered out. For this reason, we choose components exhibiting very low noise and low drifts. Critically for the long-term operation are in particular slow temperature drifts. While the power detector shows the strongest dependence on temperature, the amplifier and the voltage reference show also a slight dependence.

**PI-controller:** The output of the instrumentation amplifier is the deviation from the set point, also called the error signal, which has to be minimized in order to stabilize the microwave power. To do so, we use a PI-controller whose output sets the PIN modulator, a variable attenuator, thereby closing the feedback loop. The PI-controller constantly calculates the correction needed for the error signal to become zero. The correction is computed as a combination of one term that is proportional to the current error signal and a second term which also factors in the previous values by integrating the error signal over time.

The simplest implementation of a PI-controller is given by a single operational amplifier combined with some resistors and a capacitor as sketched in Fig. 4.2. In our case, the input signal  $U_{in}$  is given by the error signal and the output  $U_{out}$  is applied as correction to the attenuator. To check whether the circuit is functioning as desired, we can take a look at the transfer function which shows how the output voltage is influenced by the input voltage

$$T = \frac{U_{out}}{U_{in}} = -\frac{\frac{1}{i\omega C} + R2}{R1} \quad (4.1)$$

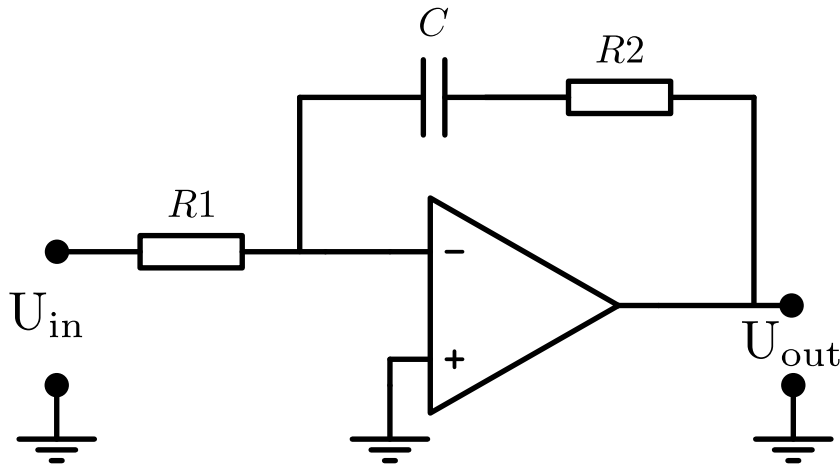


**Figure 4.2 Implementation of an analog PI-controller.** The circuit diagram shows a PI-controller consisting of a single operational amplifier. The error signal is applied as  $U_{in}$  at the inverting input while the non-inverting input is connected to ground. The output yields the correction required to minimize the error signal and due to the arrangement of the resistors and the capacitor, the output combines a term that is proportional to the current value of the input signal and a second term that is proportional to the integral of the input signal over time.

$$\Rightarrow U_{out} = -\frac{R2}{R1} U_{in} - \frac{1}{i\omega CR1} U_{in} \quad (4.2)$$

The first term in eq. (4.2), consisting of the ratio of the two resistors, describes the proportionality of  $U_{out}$  towards  $U_{in}$ , while the second term describes the integration of the input voltage over time. The dimensioning of the resistors affect how strong the proportional and integral parts are represented, while the capacity determines the time constant of the integration. The optimal values have to be determined experimentally since they depend on the particular setup in which the feedback loop is used. Here it is important to prevent the control loop of oscillating while trying to get a fast response of the output in the case that fluctuations occur in the error signal.

**PIN modulator:** The PIN modulator is a passive component which attenuates the mw signal which is passing through it. The strength of the attenuation is determined by the voltage level applied to its bias port, where 0 V causes the minimal attenuation of  $\sim -2$  dB. The output of our PI-controller can be a positive or negative voltage signal, the bias port is however only sensitive to positive voltages. For this reason, we add a DC offset onto the PI output, thereby shifting the signal completely into the positive voltage range. This is implemented on a circuit board where we also constructed a TTL switch, which allows us to put 0 V onto the bias port at any time, thereby causing the minimal attenuation. This enables us to switch off the power stabilization, which is important for the short pulses where we want the most power available, hence the smallest attenuation, and also we want to avoid the transient response of the controller during the pulses. The circuit responsible for the offset adding and the switching is given in Fig. A.2.

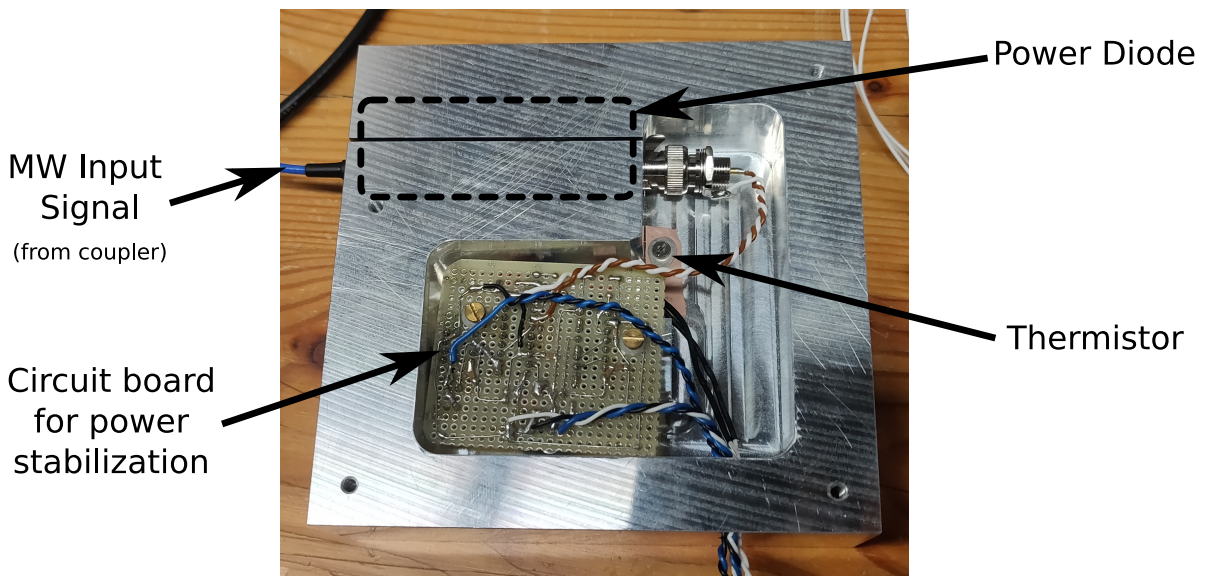


**Figure 4.3 Aluminum box for temperature stabilization.** To achieve better performance in the power stabilization feedback loop, its most critical components are placed in an temperature controlled aluminum box, which is custom-made for our purposes (see Fig. A.4 for technical drawing). Good thermal contact between the power diode and the box is assured by sliding the diode into a hole which can be narrowed by tightening a screw, thereby clamping the diode. The circuit board of the microwave power stabilization responsible for the error signal generation and the PI-controller are mounted into the box such that the housing of the voltage reference IC and the instrumentation amplifier IC are in good thermal contact with the box. During usage, the box is closed with a lid and the Peltier element is pressed against it. Also, the whole box is wrapped in hard styrofoam to isolate it from the surroundings.

### 4.2.2 Temperature stabilization

The previously described power stabilization setup is well suited to reduce noise over short time frames. For us, it is however just as important to prevent slow drifts happening over the time frame of hours and days, which often originate from temperature changes leading to voltage offsets and a slightly varying performance of certain components. The most crucial parts are the power diode, the voltage reference providing the set point and the instrumentation amplifier, as they generate and amplify the error signal. On the other hand, a slow performance change of any component that is located in front of the directional coupler in the microwave signal path should be irrelevant since the feedback loop is compensating for it.

Hence, to prevent the long-term drifts we have to focus on the components generating the error signal. For the voltage reference and the amplifier it was possible to select devices exhibiting a low drift, the power diode output on the other hand is quite temperature dependent. Therefore, we use a temperature stabilized aluminum box containing the detector as well as the circuit board with the amplifier and the PI controller. The temperature of the box is controlled by employing a second feedback loop that constantly performs the following three tasks:

1. Measuring the current temperature
2. Calculating the required correction

### 3. Heating or cooling the box

For the temperature measurement a thermistor, a resistor whose resistance changes strongly with temperature, was built into the aluminum box and was wired to a circuit board outside of the box. There the thermistor is connected to other resistors in a Wheatstone bridge, which allows an accurate measurement of the box's temperature. The set point is then defined by the values of the other resistors in the Wheatstone bridge and the received error signal is amplified and shifted into the voltage range between 0 V and 5 V.

In contrast to the power stabilization in section 4.2.1, the calculation of the correction is not received from an analog PI controller, but instead we calculate it digitally with a microcontroller. We use the "Arduino Uno Rev3" board which converts our analog error signal into a digital one and forwards it to the microchip which we programmed as a PID-controller, where the output also features a contribution that is proportional to the derivative of the error signal, additionally to the proportional and integral part.

The temperature of the box is regulated with a Peltier element which is pressed against the outside of the aluminum box with one side, while its other side is touching a heat sink. The direction of the current flow through the Peltier element determines if it is heating or cooling, while the value of the current controls the strength of the heat transfer. The Arduino has multiple digital outputs which are used to drive the Peltier element. But in order to control the box's temperature, we have to be able to apply sufficient heating power corresponding to a current of up to  $\sim 2$  A. Since the Arduino board cannot provide that, we use it to control the current strength and direction of an external voltage supply instead, where the digital Arduino outputs are used to switch several MOSFETs and Darlington transistors. The actual circuit diagram of the current control and also of the temperature measurement is shown in Fig. A.3.

By combining these three parts, the control loop is ready to regulate the temperature of the aluminum box. It is important, that the power diode and the other power stabilization components are in good thermal contact with the box. Hence, the box was fabricated especially such that these components can be clamped into the box as shown in Fig. 4.3. A technical drawing of the aluminium box is included in Fig. A.4. During operations, the box is closed with a lid and we place it inside hard styrofoam to isolate it from its surroundings, with only the heat sink looking out.

Estimating the best parameters for the PID controller manually, by improving the feedback loop's reaction to a sudden change of the temperature set point, can become impractical due to the slow time frame of temperature changes. Luckily, there are various loop tuning methods available which speed up this process, where especially the relay based tuning scheme described in [22] is suitable for us. Within that method, the PID is temporarily replaced by a simple relay such that the box is heated or cooled with fixed power, depending on its temperature being below or above the set point. The temperature of the box will then start to oscillate whereby the amplitude and the frequency are characteristic for the individual loop and can be used to calculate the optimal PID parameters. The parameters determined with this technique lead to the response of the stabilization shown in Fig. 4.4.

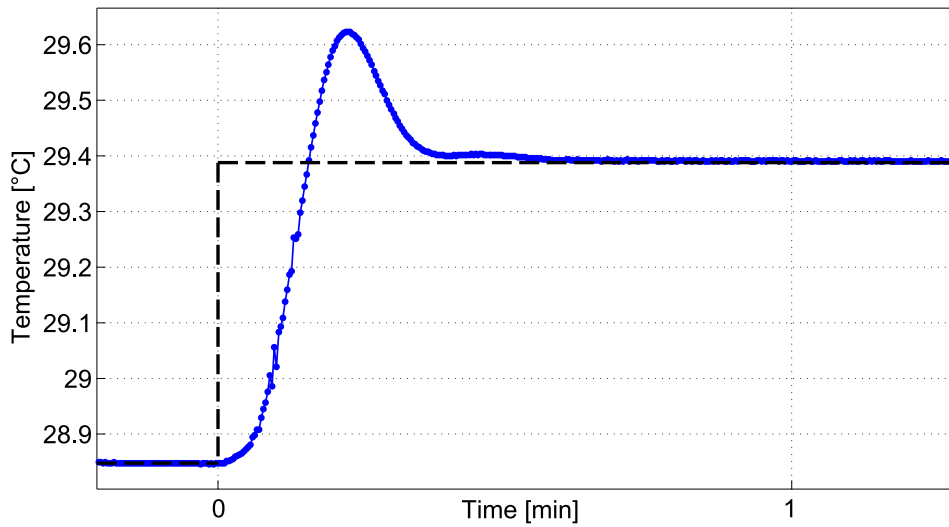


**Figure 4.4 Transient response of the temperature stabilization.** The PID parameters of the temperature stabilization were optimized using a relay based tuning scheme. The determined parameters lead to the transient response of the temperature stabilization shown here, where the blue curve is the temperature inside the box measured with the thermistor. Here, we suddenly changed the set point at  $t = 0$ , as indicated by the dashed line.

### 4.3 Noise analysis in a test setup

In order to find out which stability level we can actually reach with the power stabilization, we built a simple testing setup, shown in Fig. 4.5 a), consisting of one microwave synthesizer whose output is fed directly into the PIN modulator. Instead of the directional coupler, we then use a splitter to divide the signal into two equal parts whereof one is utilized for the correction loop while in the other part we only want to measure the microwave power with a sensitive detector. The power detection is implemented as inside the regulation loop, namely by amplifying the output of a power diode with an instrumentation amplifier relative to a fixed reference point by a factor of  $G = 1000$ . Thus the second detector and allows us to measure the microwave power independently and outside of the feedback loop, which is needed to evaluate the performance of the loop.

Now, while actively stabilizing the microwave power, we read out the power signals at the outputs of the two amplifiers with a digital oscilloscope. In Fig. 4.5 b) a single measurement of these two signals is plotted over time. The output of the power diodes can be described as the combination of a steady offset level and some fluctuations, or noise, on top of it. To estimate how robust the signal is we can compare the magnitude of the fluctuations to the magnitude of the offset level, which is defined as the stability

$$S = \frac{P_{Noise}}{P_{Signal}} = \frac{\sigma}{V_{Ref}} \quad (4.3)$$

Since we are measuring the amplified deviation of the microwave power to a fixed reference level, the noise can be calculated from the standard deviation  $\sigma$  of this signals while the offset level is directly given by the voltage reference. To get a good estimate of the noise we took a

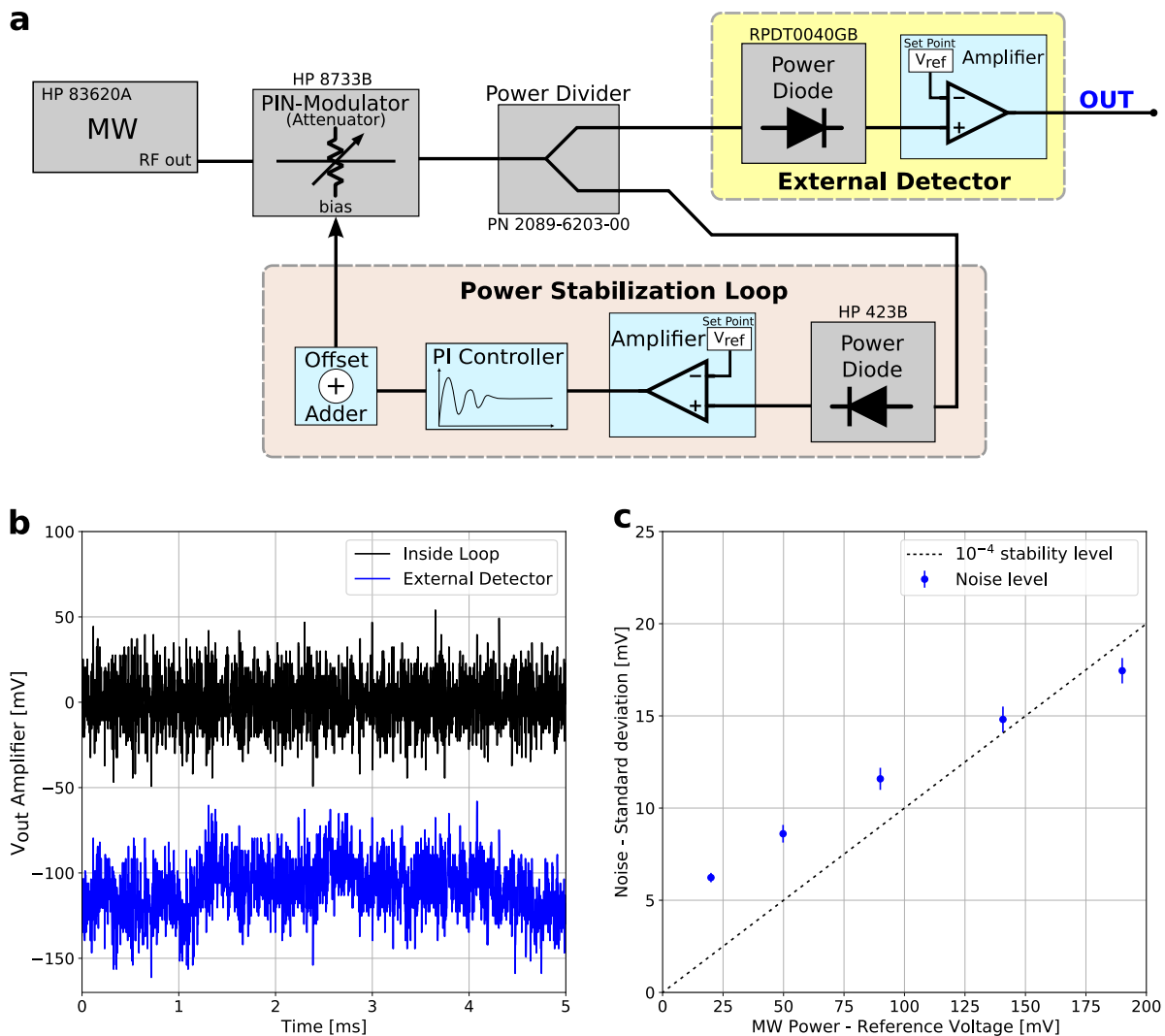


**Figure 4.5 Stability measurements in a test setup.** The setup shown in **a**) has the purpose of testing the performance of the control loop. For this, the generated microwave signal is split into two with a power divider, whereof one output is fed into the feedback loop while the other output is measured with an external detector allowing us to determine the microwave power outside of the control loop. In the detector, the mw signal is measured with a power diode and amplified with an instrumentation amplifier ( $G = 1000$ ). Panel **b**) shows a single measurement of the microwave power over 5 ms with a time resolution of  $2 \mu\text{s}$ . The two curves correspond to the microwave power inside (black curve) and outside (blue curve) of the control loop, where in each case the output of the instrumentation amplifier was recorded. Thus, the curves show the amplified deviation of the microwave power from a fixed set point. The power inside the feedback loop is centered around zero, as the PI controller tries to compensate for any deviation. The externally measured power, on the other hand, is compared to a fixed but slightly different set point, resulting in an overall offset of the blue curve which is irrelevant. Instead we focus on the fluctuations to determine the stability. In **c**) the noise level measured at the external detector is shown in dependency of the absolute power of the microwave signal, which can be adjusted by changing the set point with the voltage reference. As expected, the noise increases with increasing microwave power, however the relative size of the fluctuations and thus the stability level improves. The rightmost data point surpasses the stability level of  $10^{-4}$  which is shown by the dotted line.

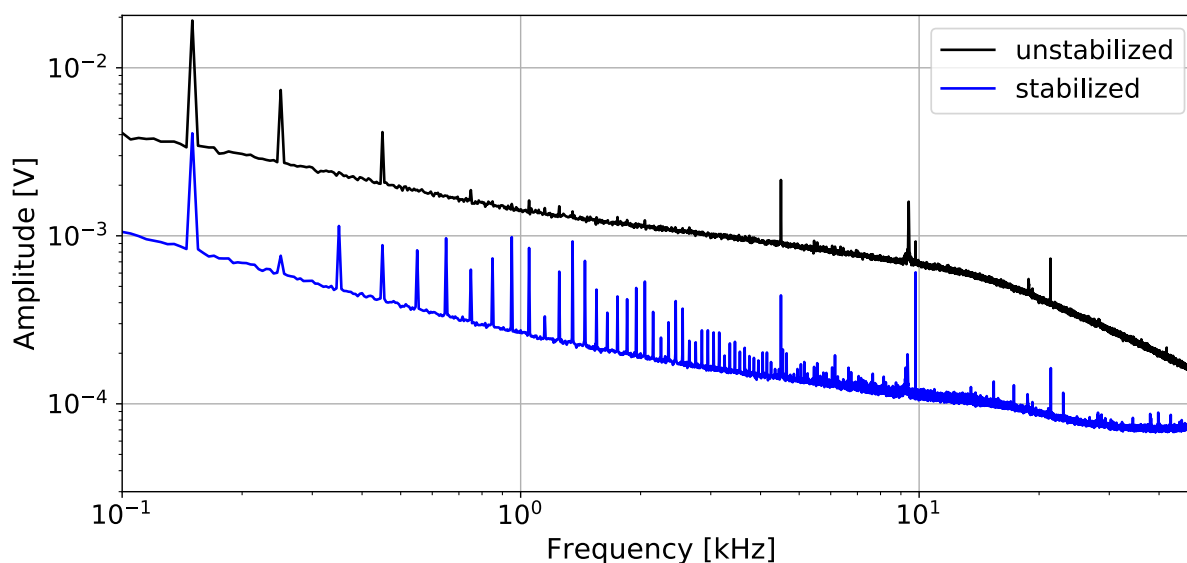


**Figure 4.6 Frequency spectrum to examine the performance of the control loop.** Measuring at the external detector with a time resolution of  $2 \mu\text{s}$ , we compare the actively stabilized signal with the unstabilized signal. For this, we opened the feedback loop by disconnecting the signal from the PIN modulator and replacing it with a constant voltage, such that the output power is on the same level as in the stabilized scenario. For both cases 1000 measurements were taken and for each one the frequency spectrum was calculated with a fast Fourier transform (FFT) algorithm. The mean of the 1000 spectra is plotted in each case, which is the reason for the smoothness of the curves. One can observe several peaks at frequencies which are multiples of 50 Hz, but the stabilization is able to reduce the noise within the entire considered frequency range.

large number of single measurements, where each one was recorded over 200 ms with a time resolution of  $2 \mu\text{s}$ , and calculated the average standard deviation. The noise determined in this way is plotted in Fig. 4.5 c) in dependency of the total microwave power of the signal, which was varied by changing the value of the voltage reference. We observe that although the noise level is increasing with microwave power, the stability level is improving and eventually reaches the target level of  $10^{-4}$ .

We would like to further analyze how much the control loop is contributing to the short-term stability achieved in the test setup. For this, we measure the power at the external detector once while actively stabilizing and a second time without stabilizing the power level. To compare these two measurements, we take a look at their frequency spectrum which is plotted in Fig. 4.6, where the spectrum is calculated for many single measurements and the average is plotted in each of the two cases. The feedback loop is able to reduce the noise across the whole frequency range. At several multiples of 50 Hz there appear peaks, which are the result of coupling of the line frequency into the electronics, for example through cables which pickup the 50 Hz oscillation from nearby devices (e.g. voltage supply) connected to the power grid. By minimizing the length of the cables we already reduced these peaks.

## Allan deviation

The Allan variance is widely applied for characterizing the frequency stability of an oscillator. Here, we will shortly introduce the Allan variance, before we apply it for our noise analysis. Let us consider a time-dependent signal  $y(t)$ , for which we introduce the time average over a duration  $\tau$  as

$$\bar{y}_k(\tau) = \frac{1}{\tau} \int_{k\tau}^{(k+1)\tau} y(t) dt \quad (4.4)$$

where  $k$  is used to index the averaged values. The Allan variance is then defined as the expectation value over all  $k$  of the variance of two consecutive time-averaged segments [23]

$$\sigma_y^2(\tau) = \mathbb{E} \left\{ \frac{1}{2} (\bar{y}_{k+1} - \bar{y}_k)^2 \right\} \quad (4.5)$$

Taking the square root of the Allan variance yields the Allan deviation

$$\sigma_y(\tau) = \sqrt{\sigma_y^2(\tau)} \quad (4.6)$$

For the noise analysis, the Allan deviation is typically evaluated as a function of the averaging time  $\tau$ . We can develop an intuitive understanding on how to interpret the Allan deviation by thinking of differently shaped signals. For instance, a signal given by some fluctuations around a constant value which are on average zero, would result in an Allan deviation which is ever decreasing for larger averaging times  $\tau$ . In this case, a longer averaging time brings the  $\bar{y}_k$  closer to the constant value, such that their difference gets smaller and with it the Allan deviation. When the signal, however, consists of fluctuations around a value that performs a random walk or slowly drifts away, it is reflected in the Allan deviation as an increase for larger values of  $\tau$ . In this manner one can identify on which timescales such features appear which is insightful for the analysis of the different noise sources contributing to the signal.

Thus far, our analysis only covered the short term behavior of the setup, as we considered single measurements taken over 200 ms. The duration as well as the time resolution may however play a substantial role for the analysis, as noise can be of different extent for different time scales and, especially for the long-term performance, slow drifts can deteriorate the reached level of stability. The Allan deviation is a good tool to investigate the behavior on the various time scales. While stabilized, we recorded the power level at the external detector over long time frames with two different measurements using a digital oscilloscope. The first was taken with only one very long trace ( $\sim 2.8$  h) with high time resolution of  $500 \mu\text{s}$ , while for the other one we constantly took short traces which were recorded in well-defined time intervals over the course of 2 days. From each of these measurements we calculated the Allan deviation and plotted it against the averaging time in Fig. 4.7. The two curves cover the Allan deviation over a broad range and show a reasonable agreement in the area where they overlap. While this allows us to analyze the noise contributions on different time scales in the test setup, we cannot transfer this knowledge to the stabilization in the final microwave setup (Fig. 4.1). This is due to some measurement limitations discussed in the following.

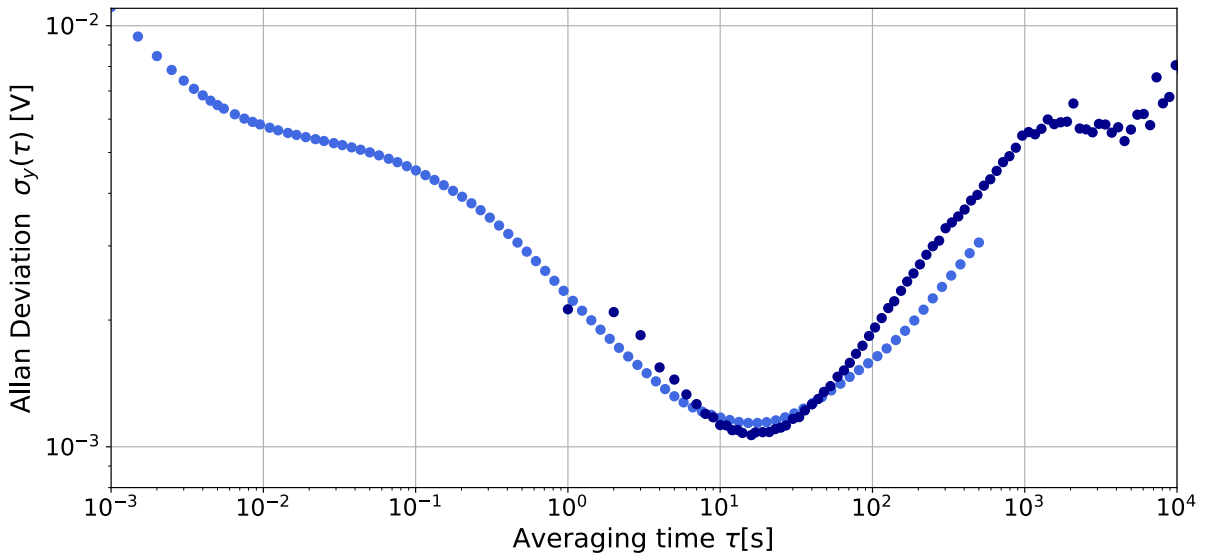


**Figure 4.7 Allan deviation of the microwave power signal.** At the external detector the power was measured over large time frames with two different procedures. For the first method, corresponding to the light blue markers, a single trace with high resolution was recorded, while for the second method many short traces were recorded over a long time frame resulting in the Allan deviation plotted with dark blue markers. In the averaging time segments covered by both curves, they agree reasonably with each other.

**Measurement limitations:** The test setup discussed in this section is useful to get an estimate for the performance of the control loop. But within the process of measuring the highly stable microwave signal, there is a significant limitation, namely the fact that the components of the external detector are noise sources themselves. Thus, during the readout of the signal an additional noise term is created, which might distort our measurement. Whether this is restricting us or not depends of course on the stability level that we want to examine, which on the other hand is ultimately restricted by the noise generated by the detector and by the finite correction capabilities of the PI-controller. Especially, since a similar combination of a power diode and an instrumentation amplifier that is used in the control loop is also used for the external detector, it is possible that the actual noise level of the signal is of similar magnitude as the readout noise that is created during the measurement. Ideally we would measure with a detector that adds a negligible noise level, however if such an excellent detector would be available to us, we would use it for the feedback loop in the first place.

More importantly, the external detector in the test setup is not temperature stabilized. Hence, with a change in ambient air temperature the external detector's output will drift, while the temperature stabilized detector in the feedback loop is insensitive to that. Especially the behavior of long-term measurements is affected by this. We believe the increase in the Allan deviation for long averaging times is mainly caused by temperature drifts, so here the drifts of the external detector are probably the dominant factor.

In the next section we will investigate the noise in the final temperature stabilized setup directly. For this, the output signal is fed to the microwave antenna in the BEC experiment, where the ultracold atoms can be used as an extremely precise detector.

## 4.4 Stability measurement with Rabi oscillations

After assuring in the previous section that the basic working principle of the microwave stabilization is functioning, we are now ready to build the feedback loop into the microwave system of the actual BEC experiment as illustrated in Fig. 4.1. Here, the stabilized microwave signal is forwarded to the antenna where oscillating magnetic fields are generated at the position of the atoms. During normal operation, the microwaves are a tool for manipulating the internal state of the BEC. For now, however, we reverse the roles and use the atoms as a precise detector to benchmark the accomplished stability. In order to obtain a sensitive measurement, the microwave fields are used to alter a specific, initial state of the atoms such that the readout yields a strong dependency on the microwave power.

A straightforward way to implement that is by Rabi oscillations (see Sec. 2.1), where the microwaves are used to resonantly couple two magnetic substates of the  $F = 1$  and  $F = 2$  manifolds. Starting with all atoms occupying a single magnetic substate, the microwaves induce the transfer to the coupled state, resulting in the oscillation of the population at the Rabi frequency  $\Omega_{mw}$  between the two states. As the square of the Rabi frequency  $\Omega_{mw}^2$  is directly proportional to the power of the microwave signal, we can draw conclusions about the performance of the feedback loop by measuring the stability of the Rabi frequency. For our purposes we chose to drive the transition between the states  $(F, m_F) = (1,0) \leftrightarrow (2,0)$ , due to the advantage of being maximally insensitive to the magnetic field as these states show no linear Zeeman shift. The disturbance of our measurement from magnetic field fluctuations are thus strongly suppressed.

The experimental sequence starts with all atoms occupying the (1,-1) state due to the trapping and cooling procedure. For the experiments described here, we also employ the optical lattice potential, which divides the atomic cloud into  $\sim 20$  individual BEC's, each consisting of roughly  $\sim 1200$  atoms. For the analysis we always considered only a single lattice site, unless it is stated otherwise. We prepare the atoms in the (1,0) state by applying two microwave  $\pi$ -pulses. During these pulses the power stabilization is turned off with the TTL-switch.

Now, the power stabilized microwave field shall be used to drive the Rabi oscillation. But a sudden activation of the control loop, would lead to a short ( $< 1$  ms) transient response of the PI controller resulting in some power fluctuations. To circumvent this, we exploit the fact that the coupling between atomic levels is highly dependent on the microwave frequency while the power diode on the other hand detects within a wide frequency range, such that the output power only weakly changes with frequency. Hence, it is possible to initially let the feedback loop stabilize itself on a frequency slightly shifted away from resonance such that the atoms are not affected and subsequently switch back to the transition frequency. Fortunately, the combination of the IQ mixer and the AWG in our setup gives high control over the frequency allowing us to easily shift the signal by 10 MHz for the first milliseconds, before we switch the already stabilized microwave signal to resonance. After driving the Rabi oscillation for a specific duration, the microwave signal is turned off and the usual absorption imaging method is used to read out the atom numbers  $N_{10}$  and  $N_{20}$  of the substates (1,0) and (2,0). From those populations we can determine the current state of the Rabi oscillation. Therefore we define the imbalance as

$$\text{Imb}(t) = \frac{N_{20}(t) - N_{10}(t)}{N_{10}(t) + N_{20}(t)} = -\cos(\Omega t) \in [-1, 1] \quad (4.7)$$

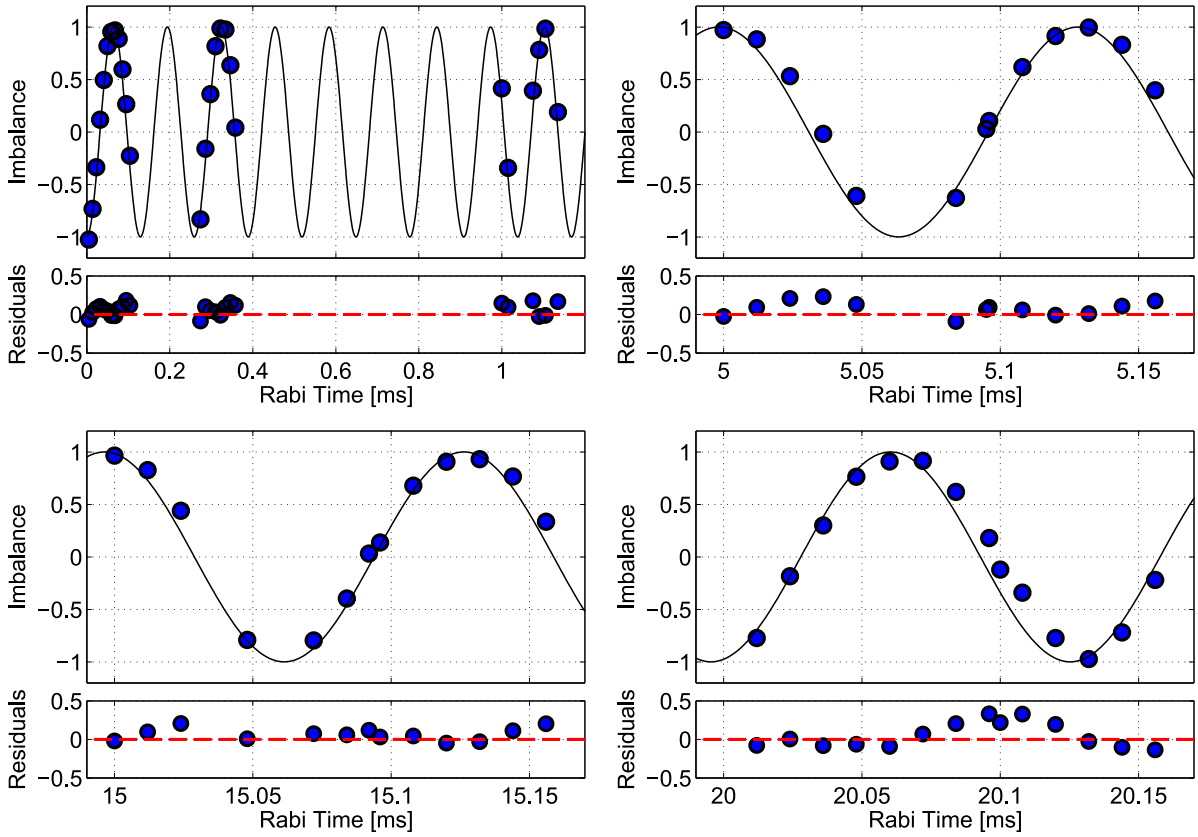


**Figure 4.8 Rabi oscillation for the microwave power stability analysis.** The transition  $(1,0) \leftrightarrow (2,0)$  was resonantly coupled for a long duration, so that up to  $\sim 270$  Rabi cycles were driven. The oscillating imbalance is plotted against the Rabi coupling time and for presentation purposes we show four temporal sections here. The solid black line is a single cosine fit going through all plots with a Rabi frequency fit parameter of  $\Omega = (7.7015 \pm 0.0003)$  kHz. The residuals corresponding to the fit are also shown for each time section.

where  $t$  is the duration of the resonant coupling and the initial state is  $\text{Imb}(t = 0) = -1$ .

The employed readout method is destructive, meaning that each experimental run the state of the atoms can be probed only once as this process simultaneously destroys the state. As a result, we cannot follow the Rabi oscillations in a single run but rather have to repeat the same sequence many times while varying the coupling duration to study the dynamics. The oscillation plotted in Fig. 4.8 was recorded by scanning the coupling time up to 35 ms which roughly corresponds to  $\sim 270$  Rabi cycles. We were able to fit all of the 270 cycles with a single cosine function, which matches the data points reasonably.

Instead of estimating the stability of the Rabi frequency from the accuracy of the fit, we measure the imbalance multiple times after a fixed coupling time  $t$  and determine the microwave stability from the width of the obtained imbalance distribution. In this way we are able to measure the shot-to-shot stability, since we repeat the same sequence. As the short-term ( $< t$ ) fluctuations of the microwave power average out over the coupling time, we measure the average Rabi frequency in each shot. The shot-to-shot fluctuations, i.e. different average Rabi frequencies in different shots, lead to the distribution of imbalance values measured after the

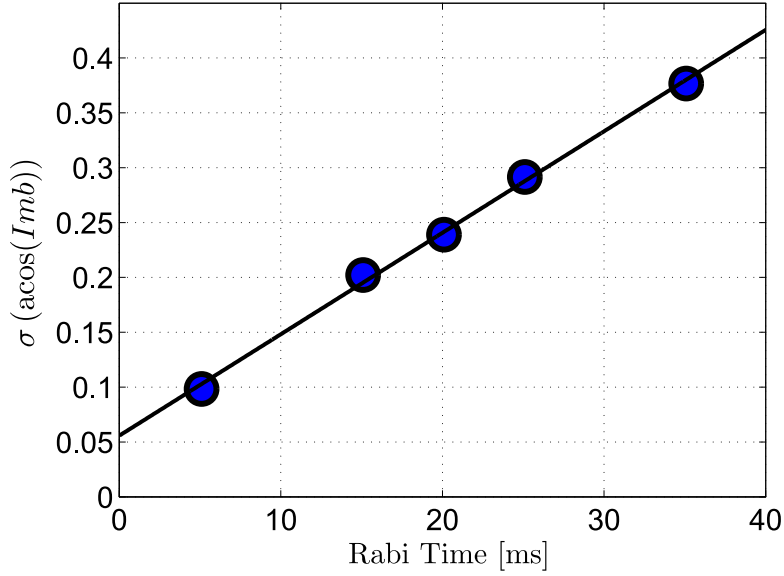


**Figure 4.9 Stability estimation of the Rabi frequency.** In the context of the Rabi oscillation displayed in Fig. 4.8 we measured the imbalance distribution for certain coupling times. Here, the width of these distributions is plotted against the coupling time, such that the slope of the linear fit is the fluctuation of the Rabi frequency and according to eq. (4.8) we calculate the stability level to be  $S = 1.91 \cdot 10^{-4}$ .

same coupling time. The width of this distribution is estimated from the average size of the imbalance fluctuations, which is given by the standard deviation  $\sigma$ . The fluctuation of the Rabi frequency is then calculated with

$$\sigma_{\Omega} = \frac{\sigma(\text{acos}(\text{Imb}(t)))}{t} \quad (4.8)$$

Assuming different average Rabi frequencies from shot-to-shot, the width of the imbalance distribution should increase linearly with the coupling time  $t$ . Hence, we expect  $\sigma_{\Omega}$  in eq. (4.8) to be time independent. For the noise analysis we have to choose the duration  $t$  sufficiently large such that the fluctuations of the imbalance values can be resolved properly. On the other hand, since the distribution of the imbalance broadens with increasing time, it will eventually stretch over the complete imbalance range, such that one cannot clearly identify to which oscillation period a data point belongs to. Hence, there is also an upper limit for the coupling time. Given these constraints, the range between 5 ms and 50 ms turned out to be suitable. We have chosen some coupling times  $t$  within this range and measured them with high statistics. For these values the numerator of eq. (4.8) was computed and plotted against  $t$  in Fig. 4.9. Since the gradient of the linear fit is  $\sigma_{\Omega}$ , we can determine the stability of the Rabi frequency to be  $S = 1.91 \cdot 10^{-4}$ . This stability corresponds to a long-term measurement, as the data points were measured over the course of several hours. Compared to the short-term stability measured in the test setup, the stability determined here is worse. In the following we will discuss possible effects which could limit the reached performance.

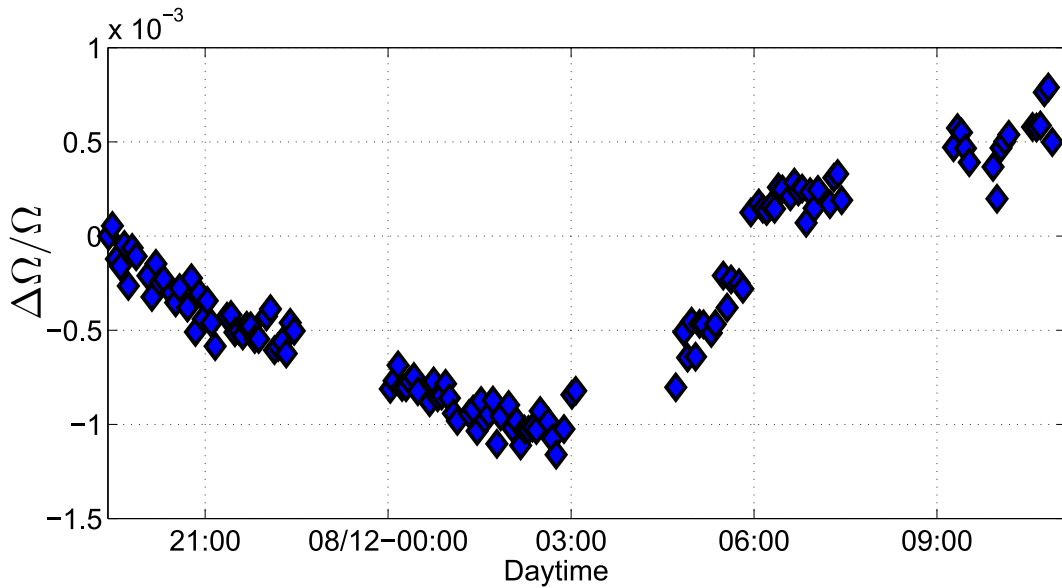


**Figure 4.10 Slow drift of the Rabi frequency.** Over a time period of  $\sim 14$  hours, Rabi oscillations between  $(1,0) \leftrightarrow (2,0)$  were driven and the imbalance value was measured after a fixed coupling time of  $t = 5.03$  ms and plotted against the daytime. Apparently, the imbalance and thus the Rabi frequency is drifting over the course of multiple hours.

#### 4.4.1 Long-term drifts

In the context of the stability analysis, the time frame of the measurement is a crucial factor. Fluctuations measured from shot-to-shot with a time difference of roughly 40 s may be of different extent and origin compared to fluctuations between data points that are taken hours or days apart. Unfortunately, we discovered that the microwave power seems to exhibit slow drifts over the course of multiple hours and days as it is shown in Fig. 4.10. Here, one can notice that the magnitude of the fluctuations over  $\sim 1$  h are significantly smaller than the magnitude of the slow drifts. Of course, this feature is also reflected in the stability analysis. There, we observe that data points taken within one hour typically lead to a stability considerably better than  $10^{-4}$ , but with increasing duration of the measurement, the slow drifts dominate and impair the stability level.

#### Origin of the slow drifts

Finding the origin of the long-term drifts in the complex setup is nontrivial. Nevertheless, we will go through the setup and try to identify possible sources for the slow drifts. Firstly, we probably can rule out the PI controller in the feedback loop, since it is operating on an entirely different timescale. Temperature changes, on the other hand, do happen on these timescales, but we already keep the most critical components inside the temperature controlled box. To estimate whether the performance of the temperature stabilization for this box is not sufficient and could be causing the drifts, we measured the imbalance after a fixed coupling time while changing the temperature set point. We then can observe, how the changing temperature affects the imbalance as shown in Fig. 4.11. From this measurement we can estimate, that

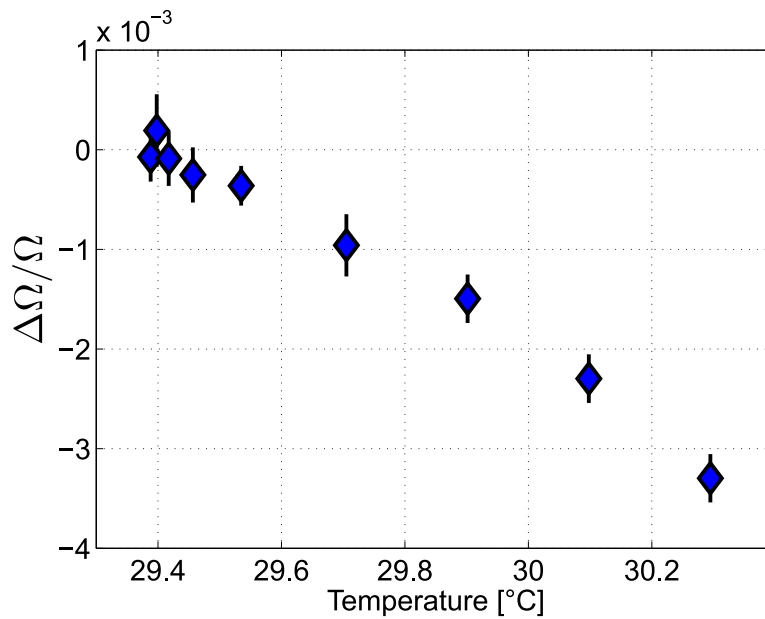


**Figure 4.11 Temperature sensitivity of the microwave power stabilization.** The imbalance was measured at a fixed Rabi coupling time of  $t = 5.04$  ms, while the temperature of the power stabilization components was changed by adjusting the set point of the temperature stabilization.

the temperature change needed to shift the microwave power to such extend is on the order of  $\sim 0.5$  K and is therefore way larger than the typical temperature fluctuations of the stabilized box which are  $< 4$  mK. The temperature stabilization was functioning properly during all measurements, so it is unlikely that this has been causing the drifts.

Going through the setup on the lookout for the cause of the slow drifts we notice again, that any component located in front of the directional coupler in the microwave setup should be irrelevant as the feedback loop is stabilizing the power at this point. Having said that, there is an important distinction one has to take into account, namely the fact that the detector measures the power of a signal over a large frequency range (0.01 to 12.4 GHz), hence the feedback loop keeps the microwave power, integrated over this whole range, constant. In contrast to that, the atoms are only influenced by microwave fields within a narrow range around the transition frequency given by the line width. For the power detected in the control loop, the strongest contribution by far is the oscillation at the atomic transition frequency, but there are also several sidebands due to mixing the initial carrier with the AWG signal at the IQ mixer. If the ratio between the power contained in the main peak compared to the power in the side peaks would change, for example due to some temperature dependent behavior of the IQ mixer, the feedback loop would still draw the overall power towards the set point. The shifted ratio, however, would result in a different amount of power contained within the line width of the atomic transition. In order to avoid this as much as possible, we adjusted the amplitude of the AWG signal to achieve a maximal sideband suppression of  $\sim 28$  dB. Nevertheless, even when the stabilization loop is working flawlessly the microwave power seen by the atoms can still vary due to a changing power fraction contained in the sidebands or due to the directional coupler branching off a slightly different amount of the signal.

It would also be possible, that the microwave signal reaching the antenna is actually stable and the observed drifts in the Rabi frequency have yet another origin. Here, physical vibrations of the experimental setup come to mind which could shift the antenna relative to the atoms. To check whether this explanation is reasonable, we physically pushed on the mount on whose end the antenna is attached to and observed the influence on the imbalance. It turned out that the relative change of the Rabi frequency due to physical displacement of the antenna is roughly  $7 \times 10^{-6} \text{ 1/}\mu\text{m}$ , so this also seems to be an unlikely source of the slow drifts. For the sake of completeness we should also mention, that a fluctuating frequency is of no concern, as the phase noise of the microwave synthesizers is on the order of  $10^{-11}$  [12]. Finally, one can also rule out the fluctuations of the magnetic field, as this shows drifts on the order of  $50 \mu\text{G}$  per hour [9], and since the magnetic field only affects the energy of the states with the quadratic Zeeman effect, this would lead to a  $1.5 \cdot 10^{-6}$  relative change of the Rabi frequency over an hour.

After discussing all kinds of possibilities for the cause of the long-term drifts, we can conclude that they are most probably driven by the change of the power ratio in the microwave spectrum. As a matter of fact, we most recently discovered a peak in the microwave spectrum at  $\sim 6 \text{ GHz}$ , which originates from the synthesizer. Using a bandpass filter it is possible to suppress this unwanted sideband, which leads to a considerable improvement of the achieved stability level. This was only discovered after this thesis was carried out, so it is not reflected in the data shown here.

#### 4.4.2 Microwave gradient

So far, we always considered a single lattice site of the standing wave trapping potential. However, the same experimental procedure is executed in all lattice sites. By analyzing all sites, we can access the spatial variation of the microwave fields along the extension of the cloud. Here, we measure the imbalance for each lattice site along the cloud and evaluate it by determining the Rabi frequency. We compare the relative change of the Rabi frequency between the lattice sites in Fig. 4.12 where we plot some single realizations and the corresponding mean. One can assume, that the variation of the Rabi frequency is caused by the form of the microwave gradient.

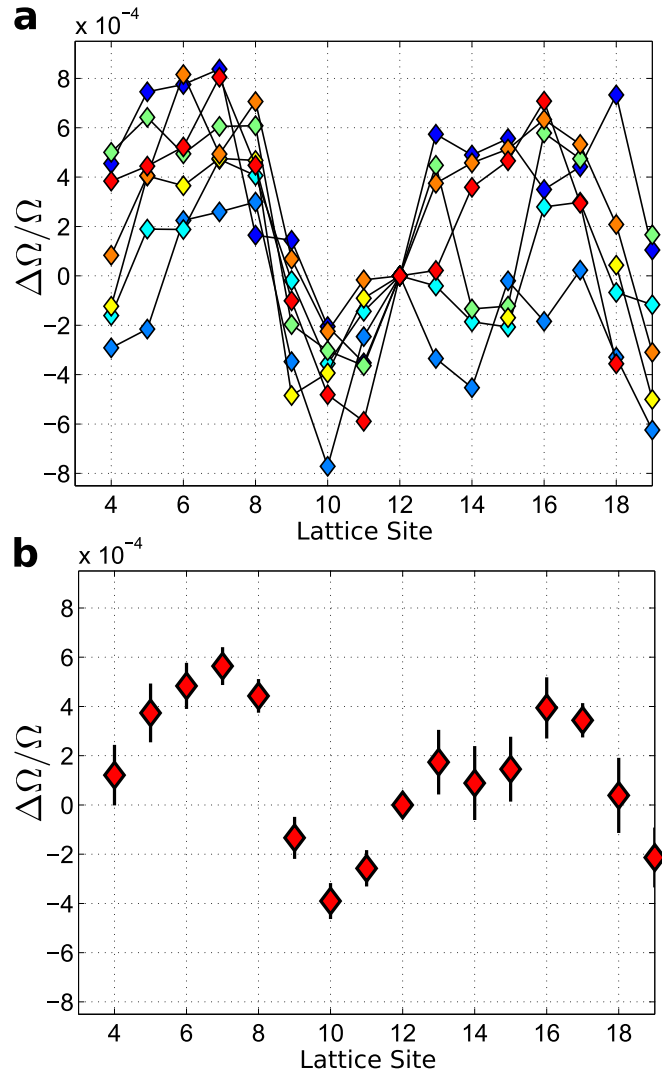


**Figure 4.12 Form of the microwave gradient.** By measuring and comparing the imbalance in all lattice sites, we can analyze how the Rabi frequency varies along the extension of the cloud. We determine the relative change of the Rabi frequency for the different lattice sites, by calculating the change relative to the 12<sup>th</sup> lattice site. In **a**), we plot several single shots indicated by the different colors. In **b**), the corresponding mean together with its error is plotted.

## 5 Impact of $q$ on the spin dynamics

In this chapter we demonstrate the role of the experimental control parameter  $q$  on the basis of two measurements. These will show the impact of  $q$  on the internal dynamics of our spin-1 BEC.

### 5.1 Spectroscopy

First, we will discuss the spectroscopy measurement, where we observe the effect of different  $q$  values on the atoms, allowing us to infer the actual value of  $q$ . This measurement serves as a calibration of the  $q$  parameter and is used in all experiments as reference, relative to which we set  $q$ . In the spectroscopy measurement we use the fact that the internal spin dynamics are strongly dependent on  $q$ , to identify the positions of phase transitions of the mean-field phase diagram shown in Fig. 3.4. A theoretical calculation of  $q$  with eq. (3.13) in contrast, only gives a rough estimate of the true value, as coupling of the mw dressing to other transitions are neglected.

The knowledge over the absolute value of  $q$  and its position in the phase diagram is required for all experiments in which the mw dressing is utilized. For instance, the quench experiments where we initiate dynamics in the system by quenching  $q$  over a phase transition, requires the knowledge over the position of the phase boundaries. In the following, we will discuss two different spectroscopy measurements.

#### Spin-changing collisions spectroscopy

Here, we use the occurrence of the spin-changing collisions as a resonance feature to identify the transition between the polar phase and the easy-plane ferromagnetic phase. For this purpose, we prepare the condensate in the polar state i.e. all atoms are in  $(1,0)$ . For this measurement, the BEC is confined in the quasi one-dimensional box-like trapping potential (no standing wave potential). Initially the mw dressing is turned off, such that  $q \sim 2\pi \times 58$  Hz and the spin-dependent interactions are strongly suppressed. We then quench the system to a different value of  $q$  by suddenly switching on the mw dressing. Subsequently, we let the system evolve for 4 s while we keep the value of  $q$  fixed. With an interaction strength of  $\sim 2\pi \times 2$  Hz, the typical time scale of spin-spin interactions is  $t_s = 0.5$  s and the evolution time is with 8  $t_s$  sufficiently long for spin dynamics to emerge. We probe this by measuring the relative population in the  $m_F = \pm 1$  states.

We carry out this sequence multiple times while quenching to different values of  $q$ . As result we observe, that a large-scale population of the  $m_F = \pm 1$  states occurs below a certain value of  $q$ . This can be identified as the phase transition between the polar phase and the

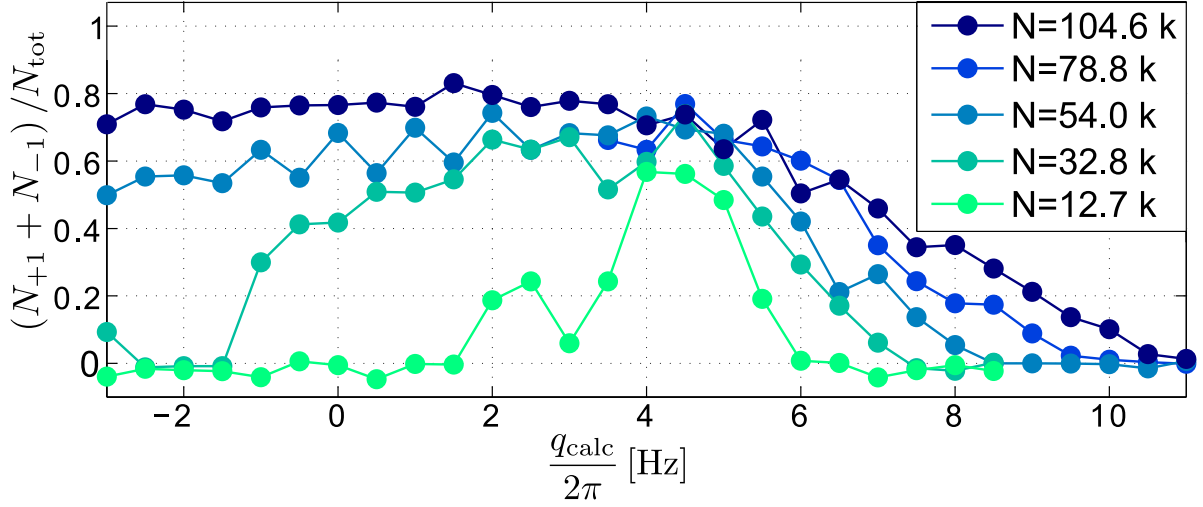


**Figure 5.1 Spin-changing collisions spectroscopy.** After preparing the system in the polar state, we quench  $q$  by switching on the mw dressing and let the system evolve for 4 s before reading out the populations of the hyperfine states in the  $z$ -projection. We plot  $(N_{+1} + N_{-1})/N_{\text{tot}}$  against  $q_{\text{calc}}$ , the value calculated with eq. (3.13). We observe a steep increase in the population of the  $m_F = \pm 1$  states when quenching to smaller values of  $q$ . This indicates the phase transition between the polar and the easy-plane ferromagnetic phase, where the spin-changing collisions start to become resonant leading to a redistribution of the population. The purpose of this measurement is to determine the shift of the calculated  $q_{\text{calc}}$  to the true value of  $q$  and therefore calibrate the experimental control parameter.

easy-plane ferromagnetic phase at  $q = -2nc_1$ , where  $n$  denotes the total density. At this value the spin-changing collisions start to become resonant leading to the steep increase in the side mode population. In the experiment, we set  $q$  through the strength of the magnetic bias field and the Rabi frequency and detuning of the mw dressing. From these values we can calculate a value  $q_{\text{calc}}$  based on eq. (3.13). This calculated value  $q_{\text{calc}}$  is set in the experiment. It is however shifted to the true value of  $q$  and the purpose of this measurement is to determine this shift. In Fig. 5.1 the relative population of the  $m_F = \pm 1$  levels is plotted against  $q_{\text{calc}}$ , where the colors indicate different total atom numbers. We observe, that the phase transition shifts towards larger  $q$  with increasing total density which is consistent with the mean-field predictions. Therefore, the spin-changing collisions spectroscopy allows us to identify the right edge of the easy-plane ferromagnetic phase at  $q = -2nc_1$ .

### $F_{\perp}$ -spectroscopy

Alternatively to the technique described above, we can also determine the position of the phase transitions with a different measurement, which we call  $F_{\perp}$ -spectroscopy. Here, we use the build-up of the transverse spin by the spin-changing collisions to obtain an reference for the true value of  $q$ . However, instead of measuring the  $F_z$ -projection, we measure the spin length in the transversal plane ( $x$ - $y$ -plane). Therefore, we read out the  $F_x$  and  $F_y$  operators simultaneously and define the spin projection in the transversal plane as  $F_{\perp} = F_x + iF_y$ . For this measurement, we also prepare the system in the polar state and quench  $q$  by switching on the mw dressing. Following an evolution time of 30 s, we readout the two transversal spin projections. Even

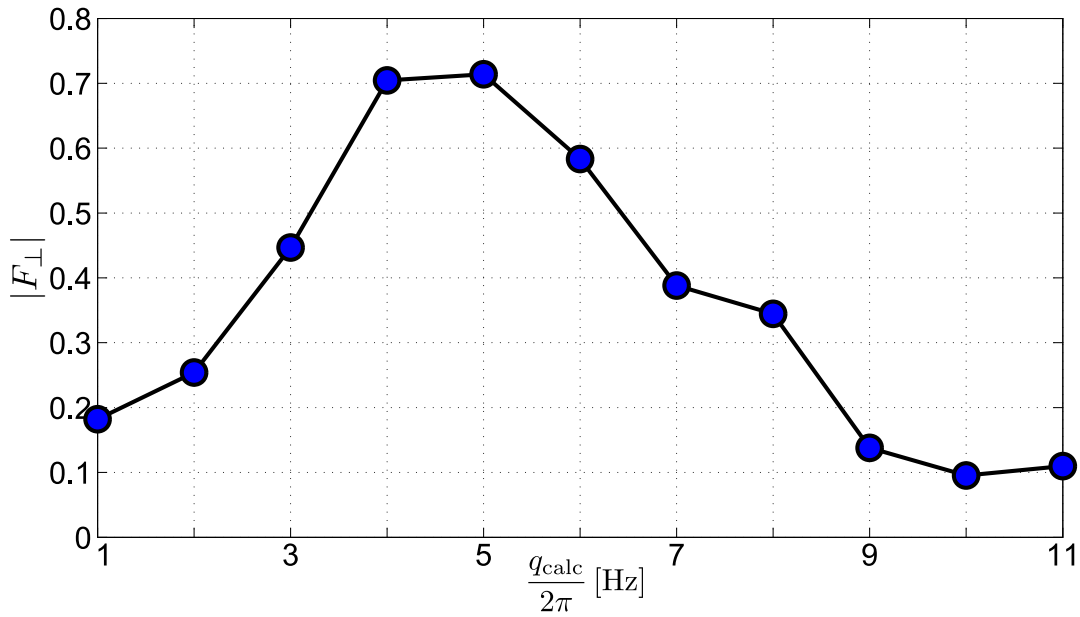


**Figure 5.2**  $F_{\perp}$ -spectroscopy. Similar to the spin-changing collisions spectroscopy, we prepare the polar state and quench  $q$ . Here, we let the system evolve for 30 s followed by a readout of the spin projection in the transversal plane. We plot the transversal spin length  $|F_{\perp}|$  against  $q$ , where we are able to recognize the easy-plane ferromagnetic phase due to its excited spin in the transversal plane.

though the system does in general not reach its final ground state, the transversal spin length already qualitatively resembles the expectations given by the mean-field ground states after 30 s of evolution time [11]. The ground state varies for the individual phases, which is reflected in the transversal spin length  $|F_{\perp}|$ . While for the polar state the expectation value of  $|F_{\perp}|$  is zero, the ground state of the easy-plane ferromagnetic phase exhibits a magnetization in the transversal plane. In Fig. 5.2 we plot the transversal spin length  $|F_{\perp}|$  against  $q_{\text{calc}}$  and we are able to recognize the easy-plane ferromagnetic phase by the excitation of the transversal spin length.

## 5.2 Gap measurement

As already mentioned in section 5.1, the system is usually not in its final mean-field ground state. Especially after quenching  $q$  over a phase transition, dynamics are initiated and the system is far from equilibrium. To describe weak excitations and fluctuations from the mean-field ground state we can utilize Bogoliubov theory. There, the basic idea is to express the field operators as the the mean-field result  $\Psi_m$  together with fluctuations  $\delta\hat{\Psi}_m$  around it.

$$\hat{\Psi}_m = \Psi_m + \delta\hat{\Psi}_m \quad (5.1)$$

For a spatially homogenous system, one usually expands the field operators in momentum space using a Fourier transformation. For our one-dimensional system we apply

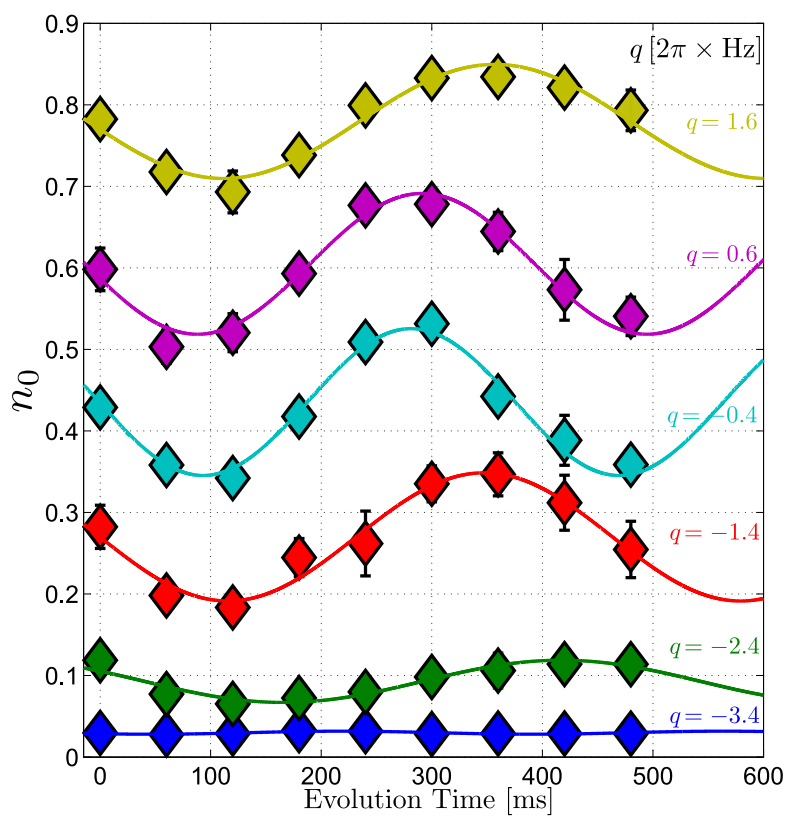


**Figure 5.3 Gapped mode oscillations.** We excite the gapped quadratic mode at  $k = 0$  by globally rotating the spinor phase with two mw  $\pi$ -pulses. Following this perturbation, we observe an oscillation in the fractional population  $n_0 = N_0/N_{\text{tot}}$ . The different colors indicate the different values of  $q$ . This measurement is also discussed in [24].

$$\hat{\Psi}_m(y) = \frac{1}{\sqrt{L}} \sum_k \hat{a}_{k,m} e^{i2\pi ky} \quad (5.2)$$

where  $L$  is the length and  $\hat{a}_{k,m}$  is the annihilation operator of a boson with momentum  $k$  in the magnetic substate  $m$ . The Bose-Einstein condensation occurs in the highly occupied zero mode ( $k = 0$ ), while the  $\hat{a}_{k \neq 0, m}$  describe the fluctuations. The ansatz (5.1) for the field operators is inserted into the Hamiltonian 3.5, which can be diagonalized using the Bogoliubov transformations. The full calculations are rather involved and can be found in [16], so we will only state some of the results which are important for our measurement. We focus on the system in the easy-plane ferromagnetic phase, where different types of excitations are described by different Bogoliubov modes. Next to Goldstone-like modes with linear dispersion at low  $k$  our system also features a Higgs-like mode, which we want to examine here. This mode exhibits a quadratic dispersion and is gapped, i.e. in the energy spectrum of this mode there is a gap at  $k = 0$ , such that a finite amount of energy is required to excite the mode even at  $k = 0$ . The theoretical expectation of the gap is given by [25]

$$\Delta = \sqrt{4n^2 c_1^2 - q^2} \quad (5.3)$$

The gap is dependent on  $q$  and vanishes at  $|q| = 2nc_1$  which marks the transition to the polar phase. The gapped mode is related to fluctuations of the transversal spin length and can be excited by globally changing the spinor phase [11]. Experimentally we prepare the polar state, quench over the phase transition to the easy-plane ferromagnetic phase and let the system evolve for 30 s. At this time, excitations in the transversal spin length have settled down. Now we excite it, however, by changing the phase of the  $m_F = 0$  component using two microwave  $\pi$ -pulses between  $(1,0) \leftrightarrow (2,0)$ . The first pulse simply transfers the population of  $(1,0)$  to the previously empty  $(2,0)$  state, while the second pulse which transfers the atoms back to  $(1,0)$ , is changed by a phase  $\Delta\phi$ . This induces a global rotation of the spinor phase. Subsequently, an oscillation in the relative population of the  $m_F = 0$  hyperfine level emerges. In Fig. 5.3 we show the dynamical evolution following the spinor phase excitation for different values of  $q$ . We observe that the oscillation frequency as well as the average fractional occupation of the  $(1,0)$  state is dependent on  $q$ . Theoretically, the  $q$ -dependence of the oscillation frequency is given by the gap eq. (5.3). For the relative population in the  $m = 0$  state, on the other hand, we expect [24]

$$n_0 = \frac{N_0}{N_{\text{tot}}} = \frac{1}{2} - \frac{q}{4nc_1} \quad (5.4)$$

Due to the conservation of the total spin in  $z$ -direction during the collisions and with the polar state as initial condition, we can assume that the side modes are equally occupied ( $N_{+1} = N_{-1}$ ) during the complete evolution. In this case the theoretical predictions can be extended in the easy-axis phase for  $-2nc_1 < q < 0$ . In Fig. 5.4 we compare the extracted oscillation frequencies and the ground state population with the theoretical expectations given by eqs. (5.3) and (5.4). Here, we assumed  $nc_1 = 2\pi \times 1.3$  Hz which defines the width of the easy-plane ferromagnetic phase. The fractional population  $n_0$  and the oscillation frequency are then in good agreement with the theoretical expectations plotted as the gray line. The oscillation frequency at  $q = -2\pi \times 3.4$  Hz shown by the blue marker disagrees with the theory prediction

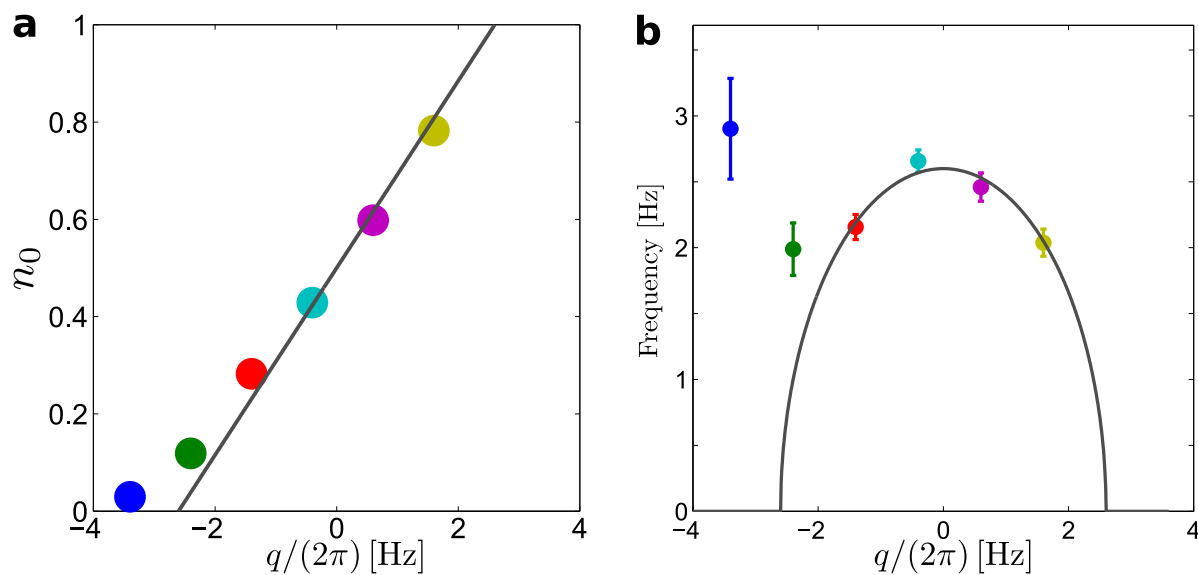


**Figure 5.4 a) Fractional population  $n_0$  and oscillation frequency** For the measurement of the gapped mode (see Fig. 5.3) we extract the average fractional population of  $m_F = 0$  and the frequency and plot them against  $q$ . The solid gray line represents the theoretical expectation as given by eqs. 5.3 and 5.4 where we assumed  $n_{c1} = 2\pi \times 1.3$  Hz. This measurement is also discussed in [24].

but this can probably be ignored, as the corresponding oscillation in Fig. 5.3 has such a small amplitude that the fit has limited significance.

## 6 Outlook

Throughout this thesis we have discussed the importance of  $q$  for our spin-1 system. Since this parameter describes the energy splitting between the  $m_F = 0$  state and the side modes in the  $F = 1$  hyperfine manifold, it is essential for the level structure of our system, and hence also determines whether the spin dependent interactions are in resonance or not. Depending on  $q$  we find different ground states within the mean-field prediction which results in separate phases. The microwave power stabilization presented in this thesis helps to achieve long-term stable operation of  $q$ .

The experimental platform allows for investigating various, physically interesting questions. Here, we will mention some of the experiments that have already been carried out and we give an outlook over some new possibilities which are available due to the better long-term stability and the increased level of control over  $q$ .

For instance, entangled particle pairs can be created by tuning the spin-changing collisions to resonance. This leads to squeezed states, where the uncertainty in one observable is reduced below the standard quantum limit, while the uncertainty of the conjugate observable is increased [8]. The entangled states can be generated in a single spatial mode and through expansion of the cloud, they can be distributed to spatially distinct regions, creating nonlocal entanglement. This was verified using the Einstein-Podolsky-Rosen steering criterion [4]. Experimentally generating and detecting entanglement requires measuring with high sensitivity such that the fluctuations below the shot-noise limit can be detected. Just as important is a high fidelity, meaning that over many repetitions the exact same initial state is prepared and the applied rf and mw fields are stable. This includes the stability of the mw dressing, as a small change of  $q$  would already worsen the ability to detect squeezing [9]. With the improved long-term stability of the microwave power, one might measure more extreme squeezing with lower fluctuations. Further, the absence of slow drifts would allow to measure over longer time frames, enabling to perform more realizations and hence measure with improved statistics.

The experiment enables also to investigate the dynamics occurring far from equilibrium in a spatial multimode scenario. To implement this, the system is quenched over a phase transition by suddenly switching on the mw dressing and thereby changing  $q$ . The ensuing dynamical evolution features self similar behavior signaling the emergence of universal dynamics, as reported in [3]. So far, we only quenched  $q$  by suddenly switching on the microwave dressing and kept it constant at a specific value for the entire evolution time. With the microwave setup described in chapter 4, however, we can also adjust the microwave dressing during the evolution time. This is made possible by changing the detuning which is controlled with an AWG. Thus, one can easily program  $q$  to change during the evolution time. This could be used to keep  $q$  in the center of the easy-plane ferromagnetic phase over the entire evolution time. The width of this phase depends on the total atomic density  $n$  which decreases over time. When we employ very long evolution times of up to 50 s, we loose around 60 % of the

---

atoms that were initially in the condensate. The phase transition to the polar phase at  $q = 2nc_1$  shifts together with the density. When quenching to the center of the easy-plane phase, one still might end up close to the phase transition to the polar phase after long evolution times due to the significant reduction of the atom number. By constantly adapting the detuning, it would be possible to get rid of this drift towards the phase transition. Alternatively to adjusting  $q$  to stay at the same position within the phase diagram, one could also utilize the high control to actively drive the system over the phase diagram in an arbitrary manner. Instead of the so far realized instantaneously fast quenches,  $q$  could also be driven adiabatically over a phase transition as in [26] to deterministically generate entangled states.

## **A Additional figures**

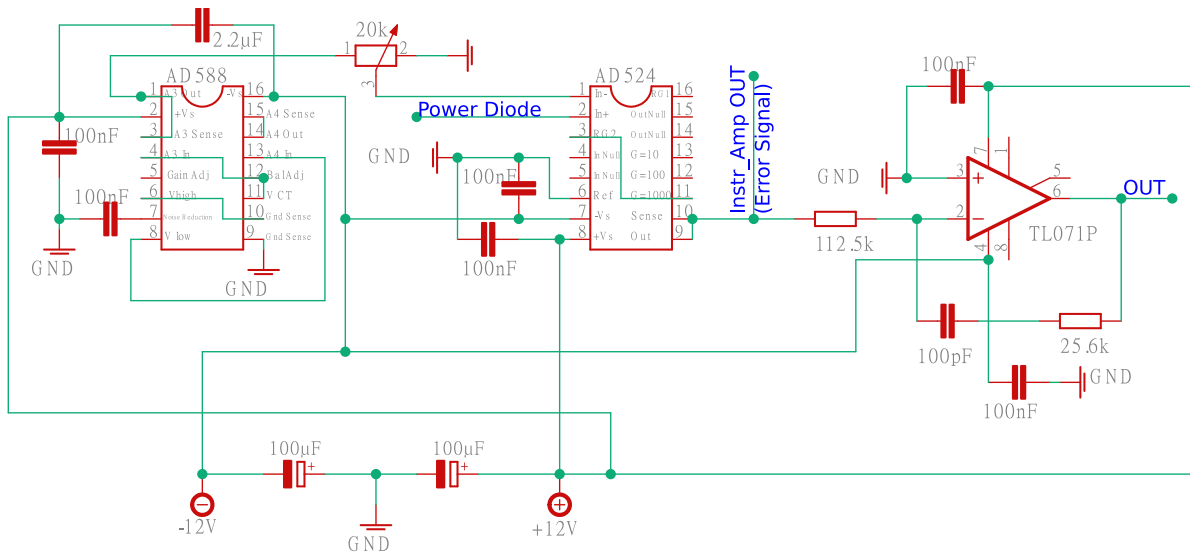


**Figure A.1** Circuit diagram of the microwave power control. The output of the power diode and the signal from a voltage reference (AD588) are used as inputs for the instrumentation amplifier (AD524) to generate the error signal. This is forwarded to a PI-controller consisting of a single operational amplifier (TL071P).

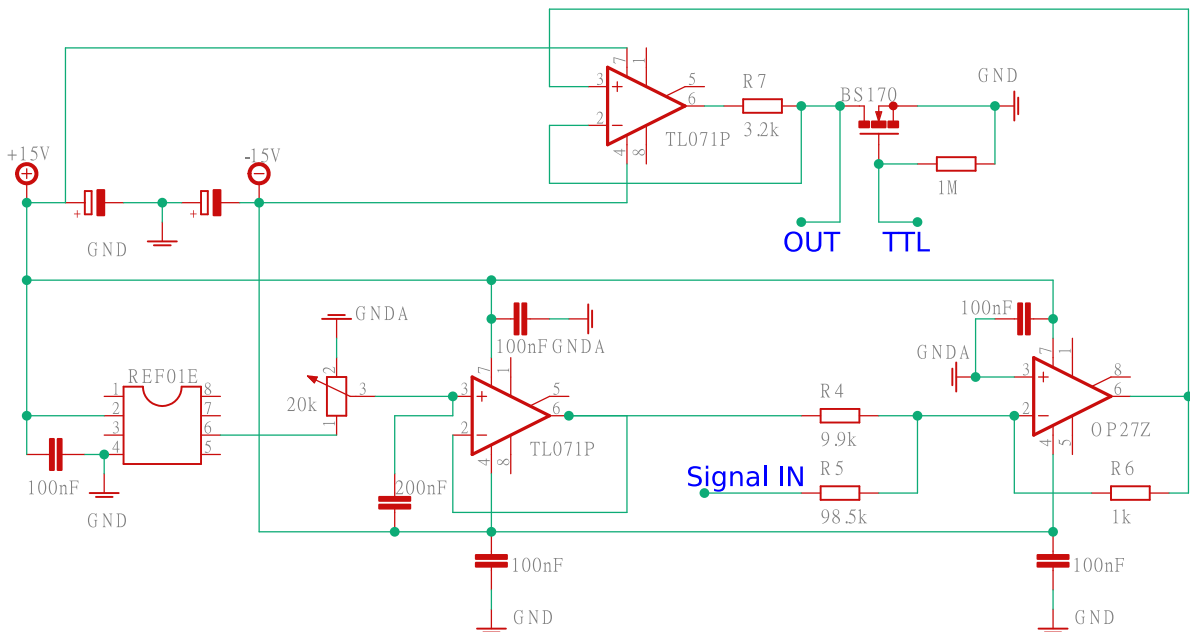


**Figure A.2** Circuit diagram for adding an offset to the control signal and to implement a TTL switch. The signal from a voltage reference (REF01E) is adjusted with a potentiometer and combined with the output of the PI-controller (Signal IN). In the upper part we realized a TTL switch.





# Bibliography

- [1] M. H. Anderson, J. R. Ensher, M. R. Matthews, C. E. Wieman, and E. A. Cornell. Observation of Bose-Einstein Condensation in a Dilute Atomic Vapor. *Science*, **269**:198–201, 1995.
- [2] K. B. Davis, M. O. Mewes, M. R. Andrews, N. J. van Druten, D. S. Durfee, D. M. Kurn, and W. Ketterle. Bose-Einstein Condensation in a Gas of Sodium Atoms. *Phys. Rev. Lett.*, **75**:3969–3973, 1995.
- [3] M. Prüfer, P. Kunkel, H. Strobel, S. Lannig, D. Linnemann, C.-M. Schmied, J. Berges, T. Gasenzer, and M. K. Oberthaler. Observation of universal dynamics in a spinor Bose gas far from equilibrium. *Nature*, **563**:217–220, 2018.
- [4] P. Kunkel, M. Prüfer, H. Strobel, D. Linnemann, A. Frölian, T. Gasenzer, M. Gärttner, and M. K. Oberthaler. Spatially distributed multipartite entanglement enables EPR steering of atomic clouds. *Science*, **360**:413–416, 2018.
- [5] M. O. Scully and M. S. Zubairy. *Quantum Optics*. Cambridge University Press, 1997.
- [6] J. Dalibard and C. Cohen-Tannoudji. Dressed-atom approach to atomic motion in laser light: the dipole force revisited. *J. Opt. Soc. Am. B*, **2**:1707–1720, 1985.
- [7] Y. Di, Y. Wang, and H. Wei. Dipole–quadrupole decomposition of two coupled spin 1 systems. *J. Phys. A: Math. Theor.*, **43**:065303, 2010.
- [8] C. D. Hamley, C. S. Gerving, T. M. Hoang, E. M. Bookjans, and M. S. Chapman. Spin-nematic squeezed vacuum in a quantum gas. *Nat. Phys.*, **8**:305–308, 2012.
- [9] Philipp Kunkel. *Splitting a Bose-Einstein condensate enables EPR steering and simultaneous readout of noncommuting observables*. PhD thesis, Heidelberg University, 2019.
- [10] P. Jordan. Der Zusammenhang der symmetrischen und linearen Gruppen und das Mehrkörperproblem. *Z. Phys.*, **94**:531–535, 1935.
- [11] Maximilian Prüfer. *Experimentally testing quantum field theory concepts with spinor Bose gases far from equilibrium*. PhD thesis, Heidelberg University, 2020.
- [12] Helmut Strobel. *Fisher Information and entanglement of non-Gaussian spin states*. PhD thesis, Heidelberg University, 2016.
- [13] Marc Robin Strohmaier. *Experimental implementation of a detection scheme for entanglement in a spinor Bose gas*. Master’s thesis, Heidelberg University, 2021.

- [14] O. Morsch and M. Oberthaler. Dynamics of Bose-Einstein condensates in optical lattices. *Rev. Mod. Phys.*, **78**:179–215, 2006.
- [15] Daniel A. Steck. Rubidium 87 D Line Data. 2003.
- [16] Y. Kawaguchi and M. Ueda. Spinor Bose–Einstein condensates. *Phys. Rep.*, **520**:253–381, 2012.
- [17] Stefan Lannig. Experimental Control of a Spin-1 Bose-Einstein Condensate. Master’s thesis, Heidelberg University, 2018.
- [18] F. Gerbier, A. Widera, S. Fölling, O. Mandel, and I. Bloch. Resonant control of spin dynamics in ultracold quantum gases by microwave dressing. *Phys. Rev. A*, **73**:041602, 2006.
- [19] S. Lannig, C.-M. Schmied, M. Prüfer, P. Kunkel, R. Strohmaier, H. Strobel, T. Gasenzer, P. G. Kevrekidis, and M. K. Oberthaler. Collisions of Three-Component Vector Solitons in Bose-Einstein Condensates. *Phys. Rev. Lett.*, **125**:170401, 2020.
- [20] G. Reinaudi, T. Lahaye, Z. Wang, and D. Guéry-Odelin. Strong saturation absorption imaging of dense clouds of ultracold atoms. *Opt. Lett.*, **32**:3143–3145, 2007.
- [21] P. Kunkel, M. Prüfer, S. Lannig, R. Rosa-Medina, A. Bonnin, M. Gärtner, H. Strobel, and M. K. Oberthaler. Simultaneous Readout of Noncommuting Collective Spin Observables beyond the Standard Quantum Limit. *Phys. Rev. Lett.*, **123**:063603, 2019.
- [22] David I. Wilson. Relay-based PID tuning. 2005.
- [23] Enrico Rubiola. *Phase Noise and Frequency Stability in Oscillators*. The Cambridge RF and Microwave Engineering Series. Cambridge University Press, 2008.
- [24] M. Prüfer, D. Spitz, S. Lannig, H. Strobel, J. Berges, and M. K. Oberthaler. Condensation and thermalization of an easy-plane ferromagnet in a spinor Bose gas. Manuscript submitted for publication.
- [25] S. Uchino, M. Kobayashi, and M. Ueda. Bogoliubov theory and Lee-Huang-Yang corrections in spin-1 and spin-2 Bose-Einstein condensates in the presence of the quadratic Zeeman effect. *Phys. Rev. A*, **81**:063632, 2010.
- [26] X.-Y. Luo, Y.-Q. Zou, L.-N. Wu, Q. Liu, M.-F. Han, M. K. Tey, and L. You. Deterministic entanglement generation from driving through quantum phase transitions. *Science*, **355**:620–623, 2017.

# Danksagung

Mit dieser Arbeit neigt sich für mich die Zeit am Rb-BEC Experiment dem Ende zu und zusätzlich schließt sie auch mein Physikstudium ab. Daher möchte ich an dieser Stelle meine Dankbarkeit für diese Möglichkeit ausdrücken und speziell die Menschen nennen, die mich in dieser Zeit unterstützt und begleitet haben.

An erster Stelle danke ich Markus Oberthaler, der mich nach meiner Bachelorarbeit nun auch wieder für meine Masterarbeit in seiner Gruppe aufgenommen hat und mir somit erneut die Gelegenheit gegeben hat in das spannende Feld der ultrakalten Gase einzutauchen. Die Kombination seiner fachlichen Expertise mit dem konstanten Interesse an neuen Fragestellungen und der hervorragenden Leitung, hat die Ausführung meiner Masterarbeit stark bereichert.

Zudem freue ich mich, dass sich Prof. Selim Jochim dazu bereit erklärt hat als Zweitgutachter dieser Arbeit zu fungieren.

Ein besonders großer Dank geht an das gesamte BEC Team. Besonders Stefan hat mir bei jeglichen physikalischen Fragestellungen gekonnt weitergeholfen und mich in den experimentellen Ablauf eingearbeitet. Es war sehr spannend das Experiment mit ihm zu betreiben und alle möglichen Probleme des Experiments zu beheben, wobei Stefan oft sehr elegante Lösungen wusste. Desweiteren möchte ich Helmut danken, der nicht nur über jedes Detail des experimentellen Aufbaus bestens Bescheid weiß, sondern auch immer sehr wertvolle Ratschläge und innovative Ideen hat. Helmut und Stefan danke ich auch besonders, für die Unterstützung beim Schreiben dieser Arbeit mittels vieler konstruktiver Ideen und wichtigen Anmerkungen. Auch Max will ich hier für die Betreuung und Zusammenarbeit danken.

Generell bin ich froh, dass die komplette SynQS Gruppe solch ein gutes Arbeitsumfeld bietet und außerdem sehr kollegial und sympatisch ist. Zudem bin ich begeistert von der feinmechanische Werkstatt. Hier danke ich David, der den Aluminiumblock für die Temperaturstabilisierung geschickt und professionell gefertigt hat.

Zu guter Letzt möchte ich mich bei meinem persönlichen Umfeld, meiner Familie und meinen Freunden bedanken, dass sie mich stets während meines kompletten Studiums begleitet haben. Ganz besonders wichtig war dabei die dauerhafte Unterstützung von meinen Eltern, die mich bei allen möglichen Problemen unterstützt haben und mich durch das gesamte Studium begleitet haben.

Außerdem möchte ich mich hier noch bei meiner Freundin Saskia bedanken, die sich stets sehr für das Laborgeschehen interessiert hat und immer für viel Freude, Unterstützung und Optimismus gesorgt hat.

# Erklärung

Ich versichere, dass ich diese Arbeit selbstständig verfasst und keine anderen als die angegebenen Quellen und Hilfsmittel benutzt habe.

Heidelberg, den 31.03.2022